haematologica
Journal of the Ferrata Storti Foundation

LILRB4 represents a promising target for immunotherapy by dual targeting tumor cells and myeloid-derived suppressive cells in multiple myeloma

by Lixin Gong, Hao Sun, Lanting Liu, Xiyue Sun, Teng Fang, Zhen Yu, Weiwei Sui, Jingyu Xu, Tingyu Wang, Fangshuo Feng, Lei Lei, Wei Rui, Yuxuan Liu, Xueqiang Zhao, Gang An, Xin Lin, Lugui Qiu, and Mu Hao

Received: January 20, 2024.
Accepted: May 20, 2024.

Citation: Lixin Gong, Hao Sun, Lanting Liu, Xiyue Sun, Teng Fang, Zhen Yu, Weiwei Sui, Jingyu Xu, Tingyu Wang, Fangshuo Feng, Lei Lei, Wei Rui, Yuxuan Liu, Xueqiang Zhao, Gang An, Xin Lin, Lugui Qiu, and Mu Hao. LILRB4 represents a promising target for immunotherapy by dual targeting tumor cells and myeloid-derived suppressive cells in multiple myeloma. Haematologica. 2024 May 30. doi: 10.3324/haematol.2024.285099 [Epub ahead of print]

LILRB4 represents a promising target for immunotherapy by dual targeting tumor cells and myeloid-derived suppressive cells in multiple myeloma

Lixin Gong[1,2,#], Hao Sun[1,2,#], Lanting Liu[1,2], Xiyue Sun[1,2], Teng Fang[1,2], Zhen Yu[1,2], Weiwei Sui[1,2], Jingyu Xu[1,2], Tingyu Wang[1,2], Fangshuo Feng[1,2], Lei Lei[3], Wei Rui[3], Yuxuan Liu[1,2], Xueqiang Zhao[4], Gang An[1,2], Xin Lin[4,*], Lugui Qiu[1,2,*], Mu Hao[1,2,*]

1. State Key Laboratory of Experimental Hematology, National Clinical Research Center for Blood Diseases, Haihe Laboratory of Cell Ecosystem, Institute of Hematology & Blood Diseases Hospital, Chinese Academy of Medical Sciences & Peking Union Medical College, Tianjin, China.

2. Tianjin Institutes of Health Science, Tianjin, China.

3. BriSTAR Immunotech Biotechnology Co. Ltd., Beijing, China.

4. Department of Basic Medical Sciences, Tsinghua University School of Medicine, Beijing, China.

Correspondence to:

Mu Hao, M.D., Ph.D., State Key Laboratory of Experimental Hematology, National Clinical Research Center for Blood Diseases, Institute of Hematology & Blood Diseases Hospital, No. 288 Nanjing Road, Tianjin 300020, China; e-mail: haomu@ihcams.ac.cn

Lugui Qiu, M.D., Ph.D., State Key Laboratory of Experimental Hematology, National Clinical Research Center for Blood Diseases, Institute of Hematology & Blood Diseases Hospital, No. 288 Nanjing Road, Tianjin 300020, China; e-mail: qiulg@ihcams.ac.cn

Xin Lin, Ph.D., Tsinghua University School of Medicine, Beijing 10084, China, email: linxin307@tsinghua.edu.cn

# contributed equally to this work

Running title: LILRB4 is a promising immunotherapy target for MM.

Data Sharing Statement: The in-house data presented in the study are deposited in the Genome Sequence Archive (GSA) repository (https://bigd.big.ac.cn/gsa-human/browse/HRA003504), BioProject ID: PRJCA013382, accession ID: HRA003504.

Authorship Contributions: LX Gong and **H Sun** contributed equally to this work. **LX Gong** and **H Sun** conducted experiments, acquired data, analyzed data, and wrote the original draft. **LT Liu and Lei L** constructed the in vivo experiment. **YX Liu** and **XY Sun** contributed to the ATAC-seq and data analysis. **T Fang, Z Yu,** and **FS Feng** contributed to data collection and data analyses. **JY Xu, WW Sui, TY Wang,** and **G An** participated in patient sample collection and clinical data analysis. **W Rui** and **XQ Zhao** constructed the STAR-T. **M Hao** contributed to conceptualization, data curation, formal analysis, methodology, project administration, supervision, and editing. **X Lin, LG Qiu, and M Hao** contributed to funding acquisition, investigation, and manuscript revision. All authors reviewed and approved the final version of the manuscript. The corresponding author attests that all listed authors meet authorship criteria and that no others meeting the criteria have been omitted.

Disclosures: none

Acknowledgments and Funding:

This research was funded by the National Natural Science Foundation of China (82341211, 82370210, and 82170194) and the CAMS Innovation Fund for Medical Sciences (CIFMS 2022-I2M1-022 and CIFMS 2021-I2M1-040). The funder has no role in study design, data collection, data analysis, interpretation, and the writing of this manuscript.

Word count:

Abstract: 247 words

Main text: 5265 words

Figure: 8

Supplementary file: 1

Abstract

Multiple myeloma (MM) remains an incurable hematological malignancy. Despite tremendous advances in the treatment, about 10% of patients still have very poor outcomes with median overall survival less than 24 months. Our study aimed to underscore the critical mechanisms pertaining to the rapid disease progression and provide novel therapeutic selection for these ultra-high-risk patients. We utilized single-cell transcriptomic sequencing to dissect the characteristic bone marrow niche of patients with survival of less than two years (EM24). Notably, an enrichment of LILRB4^{high} pre-matured plasma-cell cluster was observed in the patients in EM24 compared to patients with durable remission. This cluster exhibited aggressive proliferation and drug-resistance phenotype. High-level LILRB4 promoted MM clonogenicity and progression. Clinically, high expression of LILRB4 was correlated with poor prognosis in both newly diagnosed MM patients and relapsed/refractory MM patients. The ATAC-seq analysis identified that high chromosomal accessibility caused the elevation of LILRB4 on MM cells. CRISPR-Cas9 deletion of LILRB4 alleviated the growth of MM cells, inhibited the immunosuppressive function of MDSCs, and further rescued T cell dysfunction in MM microenvironment. The more infiltration of myeloid-derived suppressive cells (MDSCs) was observed in EM24 patients as well. Therefore, we innovatively generated a TCR-based chimeric antigen receptor (CAR) T cell, LILRB4-STAR-T. Cytotoxicity experiment demonstrated that LILRB4-STAR-T cells efficaciously eliminated tumor cells and impeded MDSCs function. In conclusion, our study elucidates that LILRB4 is an ideal biomarker and promising immunotherapy target for high-risk MM. LILRB4-STAR-T cell immunotherapy is promising against tumor cells and immunosuppressive tumor microenvironment in MM.

Keywords: multiple myeloma, single-cell RNA sequencing, LILRB4, immunotherapy

Introduction

Despite the advance of novel therapeutic agents greatly improved the outcome of MM patients in the past decades, MM is still an incurable disease. Although several studies have shown that the median overall survival (OS) has reached over ten years in newly diagnosed MM (NDMM) patients treated with bortezomib with lenalidomide and dexamethasone (VRD), about 20% to 30% of the patients survived less than 3 years.(1-3) These patients were defined as high-risk MM. Some of them with early mortality in 24 months (EM24) were regarded as ultrahigh-risk MM.(4-6) How to identify and treat high-risk patients is the major challenge in clinical practice. The main approaches to overcome the bottleneck of identifying and treating these MM patients include: first, clarifying the specific biological characteristics for ultrahigh-risk patients with the OS less than 2 years, revealing MM refractory and drug-resistant mechanisms, identifying the specific biomarkers as well as novel therapeutic targets for these ultrahigh-risk patients; second, developing new effective drugs by conducting more in-depth biological research, implementing individualized treatment strategy for these patients including prioritizing CAR-T cell therapy and bispecific antibody immunotherapy, etc.

Genome instability and immunosuppressive tumor microenvironment (iTME) are highlighted in MM disease development and progression.(7-9) Along the disease procedure, sequential genetic hits can be induced by disease progression and treatment pressure, and further increase the intra-tumoral heterogeneity of MM cells.(10) Notably, microenvironmental changes can provide a premalignant niche that precedes the acquisition of any genetic aberration.(11-14) TME is characterized by a selective reduction in cytotoxic memory T cells and an increase in several immune-suppressive cell populations, involving regulatory T cells (Treg) and myeloid-derived suppressor cells (MDSCs) in MM.(15) The crosstalk between tumor cells and the microenvironment further supports tumor growth and influences tumor evolution.(16, 17) Therefore, targeting both MM cells and the tumor-promoting microenvironment would be the ideal strategy to cure myeloma.

In this study, we investigated the heterogeneity of BMMCs at single-cell resolution from 12 NDMM patients with diverse clinical features. A LILRB4^{high} precursor plasma-cell cluster was enriched in EM24 patients and highly correlated with aggressiveness, drug resistance, and poor outcome of MM patients. LILRB4 was significantly correlated with poor outcomes of both NDMM and relapsed/refractory MM (RRMM) patients. In vitro and in vivo studies demonstrated that LILRB4 played a critical role in MM

pathogenesis. Additionally, LILRB4^{high} MM cells induced the generation of myeloid-derived suppressive cells (MDSCs). Importantly, we innovatively generated a TCR-based CAR-T cell, named STAR-T, to target LILRB4^{+} MM cells and LILRB4^{+} MDSCs. LILRB4-STAR-T cells exhibited ideal cytotoxicity against MM via targeting MM cells and MDSCs in iTME. Altogether, our study demonstrated that LILRB4 is an ultrahigh-risk gene and promising immunotherapy target via dual targeting myeloma cells and MDSCs in tumor microenvironment in MM.

Methods

The completed methods were included in the supplementary file.

Patient characteristics and scRNA-seq strategy

Bone marrow mononuclear cells (BMMCs) were obtained from 7 healthy donors (HDs) and 12 NDMM patients. The clinical and biological characteristics of 12 MM patients are listed in **Fig. S1A**. This study was conducted according to the guidelines of the Declaration of Helsinki and approved by the Institutional Ethics Review Boards of the Institute of Hematology and Blood Diseases Hospital, Chinese Academy of Medical Sciences (China) (protocol code KT2020010-EC-2). Written informed consent was obtained from all subjects involved in the study before sample collection.

Single-cell RNA sequencing and data analysis

The full process and methods for sample collection and single-cell preparation, single-cell RNA library preparation and sequencing, and scRNA-seq data processing were included in supplementary methods. Dimensionality reduction, clustering of cells, and visualization were performed according to our previous study.(14, 18) Cell cluster annotated with specific maker genes expression.

H3K27ac and H3K27me3 ChIP-seq data processing

ChIP-seq reads of H3K27ac and H3K27me3 from PRJNA608681(19) and PRJNA231147(20) were aligned to the hg19 genome using BWA (v 0.7.12). Uniquely mapped peaks and their signal intensity were obtained using MACS version 2.1.0 with default parameters. Input BAM files were used as controls, and peaks with a q-value threshold of 0.05 were considered significant. ChIPseeker(21) was utilized to identify the nearest genes around the peaks based on the transcriptional start site (TSS). Genes were considered

enriched for H3K27ac or H3K27me3 if a peak was detected up to was up to 3 kb up and downstream of the TSS.

Manufacturing of STAR-T cells

LILRB4 STAR was generated based on homemade LILRB4-specific nanobodies. The STAR-T cell structure was presented in **Fig. S7A**. Lenti-X-293T cells for lentivirus packaging were purchased from Takara Biomedical Technology Company. Lentivirus vectors (pHAGE) were used in the study. T cells were isolated using an EasySep negative selection kit (Stemcell Technologies) from peripheral blood mononuclear cells of healthy donors. T cells were first stimulated with precoated anti-CD3, anti-CD28, and human fibronectin. After being activated for 24h, T cells were transduced with concentrated virus. The transduction efficiency was determined 4 days later. T cells were cultured at a concentration of 1-3 × 10^6 cells/ml, with the culture medium half-replaced every other day during T cell expansion.(22)

In vivo study

In vivo study was performed according to our previous study. Briefly, 1 × 10^7 H929 wild-type cells were injected subcutaneously. Mice were treated with 1 × 10^7 LILRB4-STAR-T cells or mock-T cells when the average tumor size reached 100mm^3. Tumor sizes were measured every other day and calculated with formula: 0.52 × length × $width^2$ (mm^3). In vivo studies were performed in accordance with protocols approved by the Institutional Animal Care and Use Committee (IACUC) of the Institute of Hematology, Chinese Academy of Medical Sciences (Tianjin, China).

Statistical analysis

Data analyses were performed with R language and GraphPad Prism 8.0 Software. Statistical significance was set at $P < 0.05$.

Results

Single-cell transcriptomic profiling of BM ecosystem in MM patients with different clinical features

We incorporated 12 MM patients with different clinical features into this study. A single-cell transcriptomic overview of BMMCs fraction from 12 NDMM patients was compared with 7 HDs (**Fig. 1A**). Detailed clinical and pathological information of MM patients was summarized in **Fig. S1A**. Among these 12

patients, 4 patients with rapid disease progression and short survival of less than 2 years were classified as clinically ultrahigh-risk and defined as EM24 group. The other 8 patients were defined as non-EM24 (nEM24) group. PCA dimensionality reduction analysis demonstrated the significant difference in cell clustering among HDs, EM24, and nEM24 groups (**Fig. 1B**). All patients were risk stratified by ISS and R-ISS and received a combination therapy of VRD (bortezomib combined with lenalidomide and dexamethasone). All of the 4 patients in EM24 group were ISS III stage and harbored 1q+, a high-risk cytogenetic abnormality (CA).(23) Two of four EM24 patients were R-ISS III stage and presented with any two CAs of 1q+, del (17p) and t(4;14), that defined as double-hit myeloma.(24) However, in nEM24 group, five of eight patients were in ISS III stage and 3 patients were R-ISS III stage with double-hit myeloma, which simultaneously had 1q+ and t(4;14). Based on the clinical diversity of these patients, it led us to note the extensive factors affecting myeloma aggressiveness and clinical outcomes besides CAs.

In scRNAseq study, 42,936 cells were enrolled for analysis, and an average of 7,939 UMIs and 1,243 genes were generated per single cell (**Fig. S1B**). After batch-effect correction, a total of 16 diverse major BM cell types (Clusters 0-15) were identified (**Fig. 1C**), including hematopoietic stem cells (HSCs, cluster 10/*CD34*), early erythroid cells (cluster 5, 6/*GATA1*), late erythroid cells (cluster 1, 8, 12/*HBA1*), myeloid cells (cluster 4, 9, 15/CD14, *LYZ*), NK cells (cluster 2/*NKG7*), T cells (cluster 3/*CD3D*), B-cell progenitors (cluster 11/*MME*), B cells (cluster 7/*CD19*, *MS4A1*), and plasma/MM cells (cluster 0, 4, 13/*SDC1*, *TNFRSF17*) (**Fig. S1C**). The correlation of gene expression among the 16 cell clusters is shown in **Fig. S1D**.

The proportion of myeloma/plasma cells obviously elevated in MM patients compared with HDs. Notably, myeloma/plasma cells showed a stronger distribution preference in EM24 patients compared to nEM24 patients from the odds ratio (OR) analysis. Interestingly, B cells showed less distribution in EM24 patients than in nEM24 patients ($P < 0.05$), indicating the potential aberrant B-cell development and differentiation in EM24 patients. In addition, erythroid cells appeared to decrease in MM patients compared with HDs, consistent with our previous study revealing that malignant PCs could impede the erythropoiesis and result in anemia in MM.(25) Of note, a lower proportion of myeloid cells in MM patients was found. However, myeloid cells appeared to be more enriched in EM24 patients than in nEM24 patients (**Fig. 1D-1E**). Taken together, EM24 patients had a higher enrichment of MM/plasma cells and myeloid cells, whereas had a lower infiltration of T/NK cells and erythroid cells.

Enriched sub-C4 plasma cells in EM24 MM patients

We next sought to figure out the intrinsic discrepancies of MM cells between the patients in EM24 and nEM24 groups. We integrated the MM/plasma cell compartment from all samples into a joint dataset. A total of 10 heterogeneous subclusters (sub-C0-9) were identified (**Fig. 2A**). According to the light chain restriction analysis, all the clusters were light chain restricted except for sub-C7 and also highly expressed the plasma cell marker genes, including *CD38*, *SDC1*, and *TNFRSF17* (**Fig. 2B & S2A-S2B**). HD samples only harbored sub-C7 which displayed a balanced light chain ratio. Thus, we inferred that sub-C7 was the normal plasma cell cluster, and the others were the malignant plasma cells. Notably, a significant increase of sub-C4 was presented in EM24 patients compared with nEM24 patients (**Fig. 2C**). The OR analysis also confirmed that sub-C4 displayed a specifically strong distribution preference in EM24 patients (**Fig. 2D**). Importantly, we found that sub-C4 showed relatively higher level of *CD19*, *CD27* and *CD24* genes, the marker genes of initiating tumor cells in MM compared with other plasma cell subclusters, indicating a phenotypically pre-matured state of sub-C4 (**Fig. 2B & S2B**).(26) This finding suggested that EM24 patients had an enrichment of pre-matured plasma cells (sub-C4), which might be associated with the aggressive progression of EM24 patients.

Aiming to further probe the characteristics of tumor cells pertaining to the shortened survival of EM24 patients, we performed differentially expressed gene (DEG) analysis of MM cells between EM24 and nEM24 patients. There was a total of 20,711 genes from 12,835 cells. The upregulated genes in EM24 MM patients were mainly featured by sub-C4 (**Fig. S2C**). We conducted an analysis of the H3K27ac ChIP-seq data from $CD138^+$ MM cells derived from newly-diagnosed MM patients using the GSE145891 dataset. We identified genes with significant H3K27ac enrichment. Subsequently, DEG analysis was performed between the sub-C4 cluster and other MM-cell clusters. A total of 1,726 genes were observed to be up-regulated in the sub-C4 cluster. Among these up-regulated genes, 1,620 (93.86%) displayed significant H3K27ac enrichment. The top genes regulated by H3K27ac are listed in **Table S1**. Interestingly, the upregulated genes of sub-C4 were mainly regulated by H3K27ac, while the downregulated genes of sub-C4 were regulated by H3K27me3 (**Fig. 2E**).

We further inferred the differentiation stage of sub-C4 from B-cell to plasma-cell differentiation paradigm. We downloaded the publicly available scRNA-seq data of normal B-cell differentiation and BCR

information that were utilized to construct a classifier for defining B-cell differentiation stages, but not compatible for plasma cells.(27-29) Next, we integrated scRNA-seq data and scBCR-seq data of HSCs, B-cell lineage and plasma cells from HDs, and defined cell clusters along HSC to plasma-cell differentiation sequentially (**Fig. S2D to S2F**). A random-forest training approach was applied to construct a classifier that showed excellent ability to define the cell clusters of different stages from HSCs to plasma cells (all AUC value > 0.95) (**Fig.S2G**). We further generated the normal differentiation trajectory from HSCs to plasma cells following pseudo-time analysis, enabling us to map our in-house scRNAseq data of MM cells and identify the differentiation stages (**Fig. S3A&S3B**). Notably, our results showed that sub-C4 was enriched between the plasmablast stage and the terminal MM cell-cluster stage (**Fig. S3C, S3D & 2F**). Additionally, GSEA analysis of the up-regulated genes in sub-C4 showed that the signaling pathways associated with stem cell differentiation and stemness (Wnt, Notch, and Hedgehog) were significantly enriched in sub-C4 (**Fig. S3E**). These findings strongly supported that a pre-matured differentiation stage of sub-C4 MM cells was enriched in EM24 group of MM patients.

Genomic alteration and high-risk gene identification in sub-C4 plasma cell

In terms of the high proportion of pre-matured sub-C4 in BM of EM24 patients, we were interested in determining the genomic features of sub-C4 plasma cells in the pathogenesis of MM. We first utilized the publicly available proliferating and drug-resistant associated gene sets to assess the different MM subclusters.(30-33) Apparently, we found that sub-C4 plasma-cell subcluster got the highest proliferation and drug-resistance scores among the ten heterogenous MM-cell subclusters (**Fig. 3A**). Copy number variation (CNV) analysis showed that sub-C4 plasma cells exhibited the most complex CAs, including del(1p), del(2q), amp(5q), del(10q), amp(12p), del(13), del(14), del(17p), and amp(19) (**Fig. 3B**). EM24 patients also had higher CNV score than nEM24 ones (**Fig. S4A & S4B**)**.** Additionally, we found that sub-C4 plasma cells had the highest mutation score among all the MM subclusters. *KRAS*, *NRAS*, and *FAM46C*/*TENT5C* were the top mutated genes in sub-C4 plasma cells. Missense mutation was the most common mutation type (**Fig. 3C**). Consistently, further analysis showed that EM24 patients had higher mutation scores than nEM24 patients (**Fig.S4C & S4D**). The most enriched signaling pathways of sub-C4 included regulation of protein ubiquitination, immune effector processes, B cell differentiation, and cell cycle process, etc (**Fig. 3D**). We further constructed a network analysis of transcription factors (TFs) and

downstream target genes using DEGs of sub-C4 plasma cell. The result showed that *MYC* and *E2F1* were the highly activated TFs in sub-C4. *MYC* and *E2F1* were the critical TFs in regulating the lots of downstream genes and played a critical role in promoting tumor growth. Gene co-expression analysis further revealed the four gene modules, ubiquitin, and proteosome, immune-regulation, B-cell differentiation, and cell cycle, including hub genes relating with sub-C4, such as *LILRB4*, *CD74*, *XBP1*, *MKI67*, *AURKB*, *USP1* (**Fig. S4E**). Also, previous studies reported a 70 high-risk gene set (UAMS-70) and a 92 high-risk gene set in MM (SKY-92).(30, 34) Interestingly, these two gene sets had the most abundant expression in sub-C4, indicating that the sub-C4 plasma cells had the most aggressive progression ability in the heterogenous subclusters of MM cells (**Fig. S4F**).

To confirm this hypothesis, the constitution of 10 subclusters of MM/plasma cells derived from the scRNA-seq analysis was imputed in each patient of GSE2658 dataset (n=414) and MMRF-CoMMpass dataset (n=754). Survival analysis and Kaplan-Meier curve showed that patients with a high proportion of sub-C4 plasma cells had inferior outcomes (P<0.0001, **Fig. 3E & Fig. S4G**). This data supported that the proportion of sub-C4 plasma cells is a valuable prediction biomarker of the inferior outcome in NDMM patients. Furthermore, these findings also suggested that the genomic alteration in sub-C4 contributed to the aggressive progression and the poor outcome of MM patients. L1 regularization analysis was next applied to investigate specific genomic alterations within sub-C4, which were identified from the TFs-gene network and gene co-expression network.(35) We found that 7 genes were incorporated into the optimal features for discriminating the prognosis of MM patients (**Fig. S4H**). The genes were the top 7 genes with high expression levels in sub-C4 plasma cells, including *LILRB4*, *TUBA1B*, *ITGB7*, *CRIP1*, *CCND2*, *HIST1H4C,* and *CD74,* which highly correlated with the poor outcome of MM patients. Hazard ratio (HR) was calculated using both univariate and multivariate Cox proportional hazard model in MMRF-CoMMpass cohort. The HR ratio of five genes (*LILRB4*, *TUBA1B*, *ITGB7*, *CRIP1,* and *CCND2*) was higher than 1.0. (**Fig. 3F & S4I**). These data implied the prognostic value of the abundance of sub-C4 plasma cells in MM patients.

LILRB4 is a biomarker of aggressive MM

Among the 7 genes identified above, we noted that *LILRB4* was the most specifically highly expressed gene within sub-C4 **(Fig. 4A)**. To emphasize the association between *LILRB4* and the aggressive sub-C4

MM cluster, we classified plasma cells into sub-C4 and non-sub-C4 according to their expression of *LILRB4*, and generated ROC curve. The area under curve (AUC) value of sub-C4 by *LILRB4* was 0.85. At the optimal cutoff point, the sensitivity for *LILRB4* expression in distinguishing cluster reached 0.73, and the specificity reached 0.96 (**Fig. S5A**). Moreover, we found that *LILRB4* exhibited high expression in proliferation (PR) and MAF-high-level (MF) groups of MM patients (**Fig. 4B**), which represents the high-risk group in UAMS 7 groups identified by Zhan.(36) When referring to the correlation between *LILRB4* expression and disease progression, we found that *LILRB4* expression significantly increased with the progression from the precursor stage to symptomatic MM in the GEO dataset (GSE2658, GSE5900, **Fig. 4C**). Notably, patients with high *LILRB4* expression had significantly worse prognosis in both NDMM (GSE2658) and RRMM cohort (GSE57317) (**Fig. 4D**). Therefore, these clinical data further supported that *LILRB4* played a critical role in the aggressive behaviors of MM cells, resulting in the inferior outcome of patients.

Next, we confirmed the expression of *LILRB4* at protein level in MM/plasma cells from MM patients by flow cytometry. We observed that the level of ILT3, the protein for *LILRB4,* was significantly increased in precursor stage of plasma cells (pre-PC, $CD38^{+}CD138^{+}CD19^{+}CD56^{+}$) compared with mature malignant plasma cells (MPC, $CD38^{+}CD138^{+}CD19^{-}CD56^{+}$), which were both higher than normal PCs (NPC, $CD38^{+}CD138^{+}CD19^{+}CD56^{-}$) (**Fig. 4E**). Minimal residual disease (MRD) is a small number of cancer cells left in the body after treatment. These cells have the potential to come back and cause relapse in our patients. Of note, we found that the level of *LILRB4* was increased in MRD MM cells compared with NDMM cells (**Fig. 4F**). Consistently, *LILRB4* level was further increased in RRMM patients at both transcriptional and protein level (**Fig. 4F**). In MMRF-CoMMpass dataset, *LILRB4*-high patients scored higher in drug-resistance and proliferation than *LILRB4*-low patients, suggesting the possible involvement of *LILRB4* in aggressive behaviors of MM cells (**Fig. S5B**). To further investigate the biological features of *LILRB4*, we first sorted *LILRB4* positive and negative cells in MM cell lines, respectively (**Fig. S5C & 5D**). Our data showed that the endogenous LILRB4 promoted the colony formation of MM cells (**Fig. 4G**).

We further utilized CRISPR-Cas9 technology to genetically delete *LILRB4* (KO) from MM cell lines, H929 and ARP1, to detect the effects of LILRB4 in myelomagenesis. Deletion of *LILRB4* significantly suppressed the tumor growth and colony formation of MM cells (**Fig. 5A & 5B**). Additionally, *LILRB4* KO suppressed MM cell migration, promoted cell apoptosis, and increased the susceptibility to proteasome

inhibitors in MM cells (**Fig. 5C, 5D&5E**). Furthermore, the in vivo study demonstrated that tumor growth in *LILRB4*-KO group significantly decreased compared with the control ones (**Fig. 5F**). Consistently, overexpression of *LILRB4* in H929 cells notably promoted colony formation and tumor growth in vivo (**Fig. S5E & S5F**). Collectively, the highly specific gene of the aggressive sub-C4 in MM cells, *LILRB4*, was a promising biomarker of aggressive MM cells which promoted MM clonogenicity and disease progression.

Next, we intended to investigate the underlying molecular mechanisms of high *LILRB4* expression in MM cells. Based on the data shown in **Fig.3B**, amp(19) was one of the CAs in MM cells of sub-C4 and was the chromosome where *LILRB4 was* located. So we performed ATAC-seq analysis first. The results demonstrated that MM cell lines with high-level of *LILRB4* retained higher chromosomal accessibility in *LILRB4* promoter region compared with *LILRB4* low-expressed MM cells (**Fig. 6A**). According to the data shown in **Fig.2E**, the further analysis displayed significant H3K27ac enrichment in *LILRB4* promoter region in 7/10 patients (**Table. S2**). To further explore the potential transcription factors (TFs) that might regulate *LILRB4* expression, we used the hTFtarget human TFs ChIP-seq database (http://bioinfo.life.hust.edu.cn/hTFtarget/) and found that the transcription factor STAT1 could significantly bind to the *LILRB4* promoter region. The location of STAT1 ChIP-seq reads was enriched in the *LILRB4* promoter region (**Fig. 6B**). Next, we treated MM cells with STAT1-specific inhibitor, Fludarabine. Inhibition of STAT1 significantly downregulated *LILRB4* expression in MM cells (**Fig. 6C**). Of note, we co-cultured MM cells with microenvironment immune cells. We found that microenvironment cells could promote *LILRB4* expression in MM cells (**Fig. 6D**).

***LILRB4* plays a critical role in iTME in MM**

As the previous study reported, LILRB4 is an immune checkpoint on myeloid cells.(37) Except the function in promoting aggressive progression of MM cells as the above data showed, we were curious whether high-level *LILRB4* played a critical role in iTME in MM. Therefore, we downloaded the scRNA-seq data of pan-cancer myeloid cells from 45 human samples on a public available dataset and constructed a reference map using STACAS package. Myeloid cell clusters were defined as four major lineages (mast cells, DCs, monocytes, or macrophages) based on canonical gene markers. cDCs were further identified as three distinct subsets, including two classical cDC subsets ($CLEC9A^+$ cDC1s and $CD1C^+$ cDC2s) and a mature cDC subset ($LAMP3^+$ cDC). Monocytes were clustered into classical

$CD14^{hi}CD16^{-}$ monocytes (Mono-CD14), intermediate $CD14^{hi}CD16^{+}$ monocytes (Mono-CD14CD16), and non-classical $CD14^{+}CD16^{hi}$ monocytes (Mono-CD16). Interestingly, we defined MDSC by high expression of CD33, ITGAM, and CCR2. Likewise, macrophage subsets were clustered into four subsets by specific high expression of C1QC, INHBA, LYVE1, and NLRP3, respectively (**Fig. S6A to S6D**). Then, the projection of the myeloid cells in TME of our scRNA-seq data was performed onto the reference map (**Fig. 7A, 7B & S6E**).

The significantly elevated proportions of MDSC, Macro-C1QC, pDC-LILRA4, and mono-CD16 were observed in EM24 patients according to the fold change of proportion (**Fig. 7C**). Of note, MDSCs were validated to present preferential expression of genes involved in immune suppression (**Fig. 7D**). Consistently, Macro-C1QC tended to be in tumor-promoting M2 polarization state, while Macro-NLRP3 exhibited higher canonical M1 signatures. Within the DC clusters, pDC-LILRA4, which has been revealed to play a promoting role in MM progression, got the lowest activating and migratory score among four DC clusters. In monocyte compartment, $CD16^{+}$ monocytes tended to be anti-inflammatory, while $CD14^{+}$ monocytes and intermediate $CD14^{hi}CD16^{+}$ monocytes tended to be pro-inflammatory (**Fig. 7D**). The results suggested that different types of myeloid cells in EM24 MM patients contributed to severe iTME.

Given the specific *LILRB4*$^{+}$ sub-C4 of tumor cells enriched in EM24 patients and the cancer cell-to-TME communication, we characterized the phenotype of MDSCs generated by co-culture with healthy human peripheral blood mononuclear cells (PBMCs) with *LILRB4*-OE (overexpression) or EV (empty vector) MM cells in vitro. The co-culture of *LILRB4*-OE MM cells induced more generation of M-MDSCs ($CD15^{-}CD14^{+}$) compared with EV control cells. Vice versa, deletion of *LILRB4* in MM cells mitigated the generation of MDSCs from PBMCs (**Fig. 7E**). However, we did not find the induction of G-MDSCs ($CD15^{+}CD14^{-}$) in the coculture assay (data not shown). Of note, in the co-culture system, the more MDSCs induced by overexpression of *LILRB4* in MM cells promoted the greater decrease of $CD3^{+}$ T cell infiltration, and knock-out of *LILRB4* in MM cells also increased T cell infiltration (**Fig. 7E & S6F**). Consistently, we noted a decreased infiltration of MDSCs in a myeloma mouse model that harbored *LILRB4*-KO tumor cells compared with NT ones (**Fig.7F**). Collectively, the infiltration of MDSCs was efficiently induced by the enriched *LILRB4*$^{+}$ MM cells in EM24 patients. This finding further supported that *LILRB4* promoted the generation of MM-educated M-MDSC, which contributed to the iTME and MM progression.

LILRB4 is a promising immunotherapy target via dual targeting tumor cells and MDSCs in TME of MM

Besides MM cells, flow cytometry analysis confirmed that monocytic MDSCs (M-MDSCs) expressed high-level of *LILRB4* (ILT3) compared with granulocytic MDSCs (G-MDSCs) in MM patient samples (**Fig. 8A**). Given that *LILRB4* (ILT3) is a surface marker on myeloma cells as well as MDSCs, we speculated that *LILRB4* (ILT3) can be an attractive immunotherapy target in MM therapy, especially in patients with RRMM. Strikingly, we constructed a synthetic T cell receptor (TCR) and antigen receptor (STAR)-T cell targeting *LILRB4* (ILT3) positive cells, a double-chain chimeric receptor, which incorporates antigen-recognition domain of antibody and constant regions of TCR that engage endogenous CD3 signaling machinery (**Fig. S7A**).(22, 38) We investigated the cytotoxicity of LILRB4 STAR-T cell immunotherapy utilized MM cell lines, xenograft MM mouse model and primary patient samples, respectively. LILRB4 STAR-T cells or mock-T cells were co-cultured with MM cell lines, H929 and U266, at various effector: target (E: T) ratios. Compared with mock-T cells, LILRB4 STAR-T cells showed strong cytotoxicity against MM cell lines, and secreted high levels of cytokines including IFN-γ, IL-2, and TNF-α (**Fig. 8B**). LILRB4 STAR-T cells had no obvious cytotoxicity towards LILRB4 negative cells, indicating the limited off-target effect (**Fig. S7B**). The in vivo study was further performed in MM xenograft model with subcutaneous injection of H929 cells. Consistently, compared with mock-T cells treatment, LILRB4 STAR-T cells immunotherapy exhibited rapid and strong anti-MM activity (**Fig. 8C**). The survival of MM-bearing mouse was significantly extended compared with control group (undefined vs. 30 days) (**Fig. 8C**). Importantly, we did not find the obvious off-tumor toxicity, as weight and histochemical staining data showed (**Fig. S7C & S7D**).

To investigate the cytotoxicity of LILRB4 STAR-T against MDSCs, we purified the $CD14^+$ monocytes from healthy PBMCs that were used to generate M-MDSCs by adding the cocktail cytokines (**Fig.8D**).(39) M-MDSCs were then cocultured with mock-T cells or LILRB4 STAR-T cells, respectively. The specific lysis and IFN-γ cytokine secretion were significantly increased in the group of LILRB4 STAR-T treatment (**Fig. 8D**). As BCMA has been a successful immunotherapy target in MM, we investigated the association between BCMA and LILRB4 expression. We found that LILRB4 level was independent of BCMA based on the GSE2658 dataset (r=0.04, *P* = 0.28). Also, the expression of BCMA protein had no significant alteration in *LILRB4*-overexpressed MM cell lines (**Fig. S7E**). Further, the primary BMMCs from MM

patient samples, including patients receiving or not receiving BCMA-targeted immunotherapy, were isolated and treated with LILRB4 STAR-T cells at diverse E: T ratios (**Table. S3**). Based on our data shown above (**Fig.2F** and **4E**), we confirmed that $CD38^{+}LILRB4^{+}$ cells included $CD38^{+}LILRB4^{+}CD138^{high}$ and $CD38^{+}LILRB4^{+}CD138^{low}$ cell clusters in almost every MM patient. Since $CD38^{+}CD138^{high}$ is suggested to be the conventional surface marker for MM cells, we further utilized light chain restriction analysis and validated that $CD38^{+}CD138^{low}LILRB4^{+}$ cell cluster contained the clonogenic MM tumor cells (**Fig.S7F**). Strikingly, the treatment of LILRB4 STAR-T cells exhibited obvious cytotoxicity against both $CD38^{+}LILRB4^{+}$ MM cells and $CD11b^{+}LILRB4^{+}$ M-MDSCs from patients having received BCMA CAR-T therapy (**Fig. 8E**). Altogether, our study strongly supported that targeting *LILRB4* is a promising immunotherapy strategy by dual targeting MM cells and immunosuppressive MDSCs in TME of MM.

Discussion

Although long-term disease control can be achieved in a very large number of patients, the acquisition of tumor resistance leads to disease relapse, especially in patients with triple-class refractory MM (defined as resistance to immunomodulatory agents, proteasome inhibitors, and monoclonal antibodies). There is an unmet need for effective treatment options in these patients. CAR-T cell therapy is a novel approach that has demonstrated promising efficacy in the treatment of RRMM.

The interaction and co-evolution of tumor cells and microenvironment are one of the principal causes of MM refractoriness.(14) Thus, eliminating tumor cells and ameliorating microenvironment simultaneously to achieve MRD-negative is the ideal treatment strategy for MM. Our data here demonstrated an enrichment of $LILRB4^{high}$ precursor plasma-cell cluster in ultrahigh-risk patients with OS less than 2 years. This immature population was closely correlated with aggressive progression and drug resistance of MM. Recently, a high level of *LILRB4* was detected in both MM cells and myeloid cells.(40-43) However, the clinical significance and the pathophysiological function of *LILRB4* on MM has not been fully understood. *LILRB4*, an immune checkpoint on myeloid cells, has been validated to be an effective treatment target in monocytic acute myeloid leukemia (AML) and mediates AML cell migration and T cell suppression.(40) Recently, Qu et al. reported that *LILRB*4 could promote MM cell migration and was upregulated in extramedullary MM cells.(44) Here, our study demonstrated that *LILRB4* played multifaceted roles in promoting MM. High levels of *LILRB4* promoted the clonogenicity of MM cells. Deletion of *LILRB4*

efficiently alleviated tumor growth, mitigated cell migration, promoted cell apoptosis, and increased the susceptibility to proteasome inhibitors in MM cells. Importantly, our study identified that chromosomal accessibility and H3K27ac enrichment promoted LILRB4 gene transcription. Most interestingly, we indicated that tumor microenvironment could interact with MM cells and upregulate the expression of *LILRB4* in tumor cells. The regulation mechanism might involve direct or indirect cell contact. As our previous studies reported, the interaction between microenvironment cells could be accomplished by the secreted cytokines, microvesicles, or cellular metabolites.(16, 45, 46) The more precise mechanism of LILRB4 expression regulated by TME will be further explored. Generally, our results supported that the mechanisms underlying the regulation of LILRB4 expression are very complex and involve various factors and processes.

MDSCs are an important composition of iTME and play supportive roles in cancer.(47, 48) Interestingly, co-culture of *LILRB4*^{high} MM cells orchestrated the polarization of MDSCs to exhibit pro-tumor phenotypes. This further supported that the abundant MDSCs in EM24 MM patients induced a more severe immunosuppressive microenvironment. Therefore, our result supported that, *LILRB4*, the most significantly high-expressed gene in pre-matured MM population, is an attractive immunotherapy candidate target for curing MM through targeting both tumor cells and immunosuppressive microenvironment, especially for those ultrahigh-risk NDMM and RRMM patients.

Among many targets for MM immunotherapy, B cell maturation antigen (BCMA) and the orphan G protein-coupled receptor, class C group 5 member D (GPRC5D) are the most successful and matured targets. CAR-T cell therapy and bispecific T cell engagers (BiTE) targeting BCMA or GPRC5D have significantly improved the treatment response and survival for RRMM) patients.(49, 50) However, the long-term follow-up of current studies has indicated limited short-term efficacy of CAR-T cell therapy for RRMM.(51) The mechanisms underlying resistance to T-cell-based immunotherapy are complicated. BCMA and GPRC5D mainly express on matured plasma cells and MM cells.(52, 53) Current immunotherapy mostly targets mature plasma cells and is incapable of eliminating the pre-matured plasma cells or pre-B cells without expression of the target antigens, which may lead to the disease relapse and progression.(54-56) In addition, the iTME including MDSCs, can also affect the efficacy of T-cell-based immunotherapy. Our data supported high expression of *LILRB4* in plasmablasts, mature MM cells, and MDSCs, suggesting the feasibility of LILRB4-targeted immunotherapy in MM. Collectively, we

supposed that targeting *LILRB4* could eradicate potential tumor-initiating cells and impede MDSCs as well as enhance the anti-tumor effect of T-cell therapy. Based on this concept, our group innovatively designed and constructed LILRB4-targeted STAR-T cells, which incorporate antigen-recognition domain of antibodies and constant regions of TCR that engage endogenous CD3 signaling machinery. STAR-T cells can mediate strong and sensitive TCR-like signaling upon antigen stimulation.(22) In addition, STAR-T cells hold potential to reduce the risk of antigen loss-induced tumor relapse due to the high antigen sensitivity. Our result demonstrated that LILRB4 STAR-T cells show excellent cytotoxicity against tumor cells and MDSCs, respectively, and extend the survival of myeloma-bearing mice. We did not find the off-tumor cytotoxicity in vivo as well. Recently a bispecific T cell engager targeting *LILRB4* has also shown potent killing effects toward MM cells.(43) Hence, *LILRB4* is an attractive immunotherapy target with promising prospects for development and application. Based on this study, we have set up an investigator-initiated trial (IIT) to explore the safety and efficacy of LILRB4 STAR-T cells in RRMM (Clinical Trial: NCT05913804). More evidence for the feasibility and underlying mechanisms for LILRB4-STAR-T immunotherapy in MM is under investigation.

In conclusion, our study delineated that LILRB4 is an ideal biomarker for identification of high-risk MM, and represents a promising target for MM immunotherapeutics by dual targeting tumor cells and myeloid-derived suppressive cells in MM. Strikingly, our findings further suggested that combining the treatment of LILRB4-STAR-T would be an attractive strategy for RRMM with BCMA targeting therapy.

References

1. Bazarbachi AH, Al Hamed R, Malard F, et al. Relapsed refractory multiple myeloma: a comprehensive overview. Leukemia. 2019;33(10):2343-2357.

2. Kumar S, Baizer L, Callander NS, et al. Gaps and opportunities in the treatment of relapsed-refractory multiple myeloma: Consensus recommendations of the NCI Multiple Myeloma Steering Committee. Blood Cancer J. 2022;12(6):98.

3. Cowan AJ, Green DJ, Kwok M, et al. Diagnosis and Management of Multiple Myeloma: A Review. JAMA. 2022;327(5):464-477.

4. Sonneveld P, Avet-Loiseau H, Lonial S, et al. Treatment of multiple myeloma with high-risk cytogenetics: a consensus of the International Myeloma Working Group. Blood. 2016;127(24):2955-2962.

5. Ríos-Tamayo R, Sáinz J, Martínez-López J, et al. Early mortality in multiple myeloma: the time-dependent impact of comorbidity: A population-based study in 621 real-life patients. Am J Hematol. 2016;91(7):700-704.

6. Terebelo H, Srinivasan S, Narang M, et al. Recognition of early mortality in multiple myeloma by a prediction matrix. Am J Hematol. 2017;92(9):915-923.

7. Neuse CJ, Lomas OC, Schliemann C, et al. Genome instability in multiple myeloma. Leukemia. 2020;34(11):2887-2897.

8. Tirier SM, Mallm JP, Steiger S, et al. Subclone-specific microenvironmental impact and drug response in refractory multiple myeloma revealed by single-cell transcriptomics. Nat Commun. 2021;12(1):6960.

9. Kumar SK, Rajkumar SV. The multiple myelomas - current concepts in cytogenetic classification and therapy. Nat Rev Clin Oncol. 2018;15(7):409-421.

10. Yan Y, Qin X, Liu J, et al. Clonal phylogeny and evolution of critical cytogenetic aberrations in multiple myeloma at single-cell level by QM-FISH. Blood Adv. 2022;6(2):441-451.

11. Pawlyn C, Morgan GJ. Evolutionary biology of high-risk multiple myeloma. Nat Rev Cancer. 2017;17(9):543-556.

12. Liu R, Gao Q, Foltz SM, et al. Co-evolution of tumor and immune cells during progression of multiple myeloma. Nat Commun. 2021;12(1):2559.

13. Dutta AK, Alberge JB, Sklavenitis-Pistofidis R, et al. Single-cell profiling of tumour evolution in multiple myeloma - opportunities for precision medicine. Nat Rev Clin Oncol. 2022;19(4):223-236.

14. Lv J, Sun H, Gong L, et al. Aberrant metabolic processes promote the immunosuppressive microenvironment in multiple myeloma. Front Immunol. 2022;13:1077768.

15. Zavidij O, Haradhvala NJ, Mouhieddine TH, et al. Single-cell RNA sequencing reveals compromised immune microenvironment in precursor stages of multiple myeloma. Nat Cancer. 2020;1(5):493-506.

16. Hao M, Zhang L, An G, et al. Suppressing miRNA-15a/-16 expression by interleukin-6 enhances drug-resistance in myeloma cells. J Hematol Oncol. 2011;4:37.

17. Hao M, Zhang L, An G, et al. Bone marrow stromal cells protect myeloma cells from bortezomib induced apoptosis by suppressing microRNA-15a expression. Leuk Lymphoma. 2011;52(9):1787-1794.

18. Sun H, Fang T, Wang T, et al. Single-cell profiles reveal tumor cell heterogeneity and immunosuppressive microenvironment in Waldenström macroglobulinemia. J Transl Med. 2022;20(1):576.

19. Jia Y, Zhou J, Tan TK, et al. Myeloma-specific superenhancers affect genes of biological and clinical relevance in myeloma. Blood Cancer J. 2021;11(2):32.

20. Agarwal P, Alzrigat M, Párraga AA, et al. Genome-wide profiling of histone H3 lysine 27 and lysine 4 trimethylation in multiple myeloma reveals the importance of Polycomb gene targeting and highlights EZH2 as a potential therapeutic target. Oncotarget. 2016;7(6):6809-6823.

21. Yu G, Wang LG, He QY. ChIPseeker: an R/Bioconductor package for ChIP peak annotation, comparison and visualization. Bioinformatics. 2015;31(14):2382-2383.

22. Liu Y, Liu G, Wang J, et al. Chimeric STAR receptors using TCR machinery mediate robust responses against solid tumors. Sci Transl Med. 2021;13(586):eabb5191.

23. An G, Xu Y, Shi L, et al. Chromosome 1q21 gains confer inferior outcomes in multiple myeloma treated with bortezomib but copy number variation and percentage of plasma cells involved have no additional prognostic value. Haematologica. 2014;99(2):353-359.

24. Rajkumar SV. Multiple myeloma: 2022 update on diagnosis, risk stratification, and management. Am J Hematol 2022;97(8):1086-1107.

25. Liu L, Yu Z, Cheng H, et al. Multiple myeloma hinders erythropoiesis and causes anaemia owing to high levels of CCL3 in the bone marrow microenvironment. Sci Rep. 2020;10(1):20508.

26. Gao M, Bai H, Jethava, Y, et al. Identification and Characterization of Tumor-Initiating Cells in Multiple Myeloma. J Natl Cancer Inst. 2020;112(5):507-515.

27. Caron M, St-Onge P, Sontag T, et al. Single-cell analysis of childhood leukemia reveals a link between developmental states and ribosomal protein expression as a source of intra-individual heterogeneity. Sci Rep. 2020;10(1):8079.

28. Mehtonen J, Teppo S, Lahnalampi M, et al. Single cell characterization of B-lymphoid differentiation and leukemic cell states during chemotherapy in ETV6-RUNX1-positive pediatric leukemia identifies drug-targetable transcription factor activities. Genome Med. 2020;12(1):99.

29. Zhang Y, Wang S, Zhang J, et al. Elucidating minimal residual disease of paediatric B-cell acute lymphoblastic leukaemia by single-cell analysis. Nat Cell Biol. 2022;24(2):242-252.

30. Shaughnessy JD Jr., Zhan F, Burington BE, et al. A validated gene expression model of high-risk multiple myeloma is defined by deregulated expression of genes mapping to chromosome 1. Blood. 2007;109(6):2276-2284.

31. Zhou W, Yang Y, Xia J, et al. NEK2 induces drug resistance mainly through activation of efflux drug pumps and is associated with poor prognosis in myeloma and other cancers. Cancer Cell. 2013;23(1):48-62.

32. Hao M, Franqui-Machin R, Xu H, et al. NEK2 induces osteoclast differentiation and bone destruction via heparanase in multiple myeloma. Leukemia. 2017;31(7):1648-1650.

33. Franqui-Machin R, Hao M, Bai H, et al. Destabilizing NEK2 overcomes resistance to proteasome inhibition in multiple myeloma. J Clin Invest. 2018;128(7):2877-2893.

34. Kuiper R, Broyl A, de Knegt Y, et al. A gene expression signature for high-risk multiple myeloma. Leukemia. 2012;26(11):2406-2413.

35. Steiert B, Timmer J, Kreutz C. L1 regularization facilitates detection of cell type-specific parameters in dynamical systems. Bioinformatics. 2016;32(17):i718-i726.

36. Zhan F, Huang Y, Colla S, et al. The molecular classification of multiple myeloma. Blood. 2006;108(6):2020-2028.

37. Yang T, Qian Y, Liang X, et al. LILRB4, an immune checkpoint on myeloid cells. Blood Sci. 2022;4(2):49-56.

38. Wang J, Zhang X, Zhou Z, et al. A novel adoptive synthetic TCR and antigen receptor (STAR) T-Cell therapy for B-Cell acute lymphoblastic leukemia. Am J Hematol. 2022;97(8):992-1004.

39. Bancaro N, Calì B, Troiani M, et al. Apolipoprotein E induces pathogenic senescent-like myeloid cells in prostate cancer. Cancer Cell. 2023;41(3):602-619.

40. Deng M, Gui X, Kim J, et al. LILRB4 signalling in leukaemia cells mediates T cell suppression and tumour infiltration. Nature. 2018;562(7728):605-609.

41. Zurli V, Wimmer G, Cattaneo F, et al. Ectopic ILT3 controls BCR-dependent activation of Akt in B-cell chronic lymphocytic leukemia. Blood. 2017;130(18):2006-2017.

42. Li J, Gao A, Zhang F, et al. ILT3 promotes tumor cell motility and angiogenesis in non-small cell lung cancer. Cancer Lett. 2021;501:263-276.

43. Di Meo F, Iyer A, Akama K, et al. A target discovery pipeline identified ILT3 as a target for immunotherapy of multiple myeloma. Cell Rep Med. 2023;4(7):101110.

44. Sun Z, Ji J, Li Y, et al. Identification of evolutionary mechanisms of myelomatous effusion by single-cell RNA sequencing. Blood Adv. 2023;7(15):4148-4159.

45. Yu T, Du C, Ma X, et al. Polycomb-like Protein 3 Induces Proliferation and Drug Resistance in Multiple Myeloma and Is Regulated by miRNA-15a. Mol Cancer Res. 2020;18(7):1063-1073.

46. Wei X, Yu Z, Tang P, et al. Multiple myeloma-derived miR-27b-3p facilitates tumour progression via promoting tumour cell proliferation and immunosuppressive microenvironment. Clin Transl Med. 2023;13(1):e1140.

47. Li K, Shi H, Zhang B, et al. Myeloid-derived suppressor cells as immunosuppressive regulators and therapeutic targets in cancer. Signal Transduct Target Ther. 2021;6(1):362.

48. Veglia F, Sanseviero E, Gabrilovich DI. Myeloid-derived suppressor cells in the era of increasing myeloid cell diversity. Nat Rev Immunol. 2021;21(8):485-498.

49. Wang D, Wang J, Hu G, et al. A phase 1 study of a novel fully human BCMA-targeting CAR (CT103A) in patients with relapsed/refractory multiple myeloma. Blood. 2021;137(21):2890-2901.

50. Mailankody S, Devlin SM, Landa J, et al. GPRC5D-Targeted CAR T Cells for Myeloma. N Engl J Med. 2022;387(13):1196-1206.

51. Lee LSH, Yong KL. BCMA CARs in multiple myeloma: room for more? Blood. 2021;137(21):2859-2860.

52. van de Donk N, Usmani SZ, Yong K. CAR T-cell therapy for multiple myeloma: state of the art and prospects. Lancet Haematol. 2021;8(6):e446-e461.

53. Cappell KM, Kochenderfer JN. Long-term outcomes following CAR T cell therapy: what we know so far. Nat Rev Clin Oncol. 2023;20(6):359-371.

54. Raje N, Berdeja J, Lin Y, et al. Anti-BCMA CAR T-Cell Therapy bb2121 in Relapsed or Refractory Multiple Myeloma. N Engl J Med. 2019;380(18):1726-1737.

55. Smith EL, Harrington K, Staehr M, et al. GPRC5D is a target for the immunotherapy of multiple myeloma with rationally designed CAR T cells. Sci Transl Med. 2019;11(485):eaau7746.

56. Mikkilineni L, Kochenderfer JN. CAR T cell therapies for patients with multiple myeloma. Nat Rev Clin Oncol. 2021;18(2):71-84.

Figure legends

Fig. 1 | Single-cell transcriptomics profiling of bone marrow ecosystem in MM patients

(A) Schematic representation of the experimental strategy based on in-house and outsourced data. Bone marrow mononuclear cells (BMMCs) from 7 healthy donors (HD), 4 multiple myeloma (MM) patients with early death (EM24), and 8 without early death (nEM24) were measured by 10× Genomics-based scRNA-Seq. Multi-omics data and biological assays were applied to validate our findings.

(B) Two-dimensional plots showing the distribution of each sample. The point color indicates sample group. Triangles represent the median of principal component analysis (PCA).

(C) Uniform manifold approximation and projection (UMAP) plots showing cell clusters (left panel) and cell annotation (right panel) by color.

(D) UMAP projections of cells from each sample. Sample names and sample groups are labeled in the figure.

(E) Bubble plots showing the proportion of each cell type in each sample (top). Samples were divided into EM24 MM patients (red), nEM24 MM patients (blue), and HD (gray). Heatmap plot illustrating the odd ratios (OR) of each cell in each sample group based on Fisher's exact test (bottom). A high OR with an asterisk represents the cell is more preferred to distribute in the group, while a low OR with an asterisk represents the cell is less preferred to distribute in the group.

Fig. 2 | Characteristics of plasma cells in EM24 MM patients

(A) Uniform manifold approximation and projection (UMAP) plot showing 10 plasma cell clusters from all samples.

(B) UMAP plots showing the expression of marker genes in plasma cells.

(C) UMAP plots showing the plasma cells originated from healthy donors (HDs), patients with early death. (EM24), and patients without early death (nEM24).

(D) Heatmap plot illustrating the odds ratio (OR) of each cluster in each sample group based on Fisher's exact test (top). Bar plot showing the proportion of each cluster in each multiple myeloma (MM) sample and HD (bottom).

(E) T-distributed stochastic neighbor embedding (tSNE) point and density plots showing the distribution of epigenetic-controlled genes (top). Fitted density plot illustrating the H3K27ac-regulated and H3K27me3-regulated gene signal from ChIP-seq data (bottom).

(F) Density line plot showing the cell distribution of plasma-cell lineage along with the pseudotime. HSC: hematopoietic stem cells, MPP: multipotent blood progenitors.

Fig. 3 | Genomic alteration and high-risk gene identification in sub-C4 plasma cell

(A) Violin plots showing the cell score of proliferation and drug resistance in multiple myeloma (MM) cell clusters.

(B) Circular genomic map illustrating the copy number variations in MM cell clusters. Each lane indicates one cell cluster and the outmost lane indicates chromosome structure. Red represents amplification and blue represents deletion.

(C) Waterfall plot displaying 63 mutational driver genes in 947 MM patients of MMRF-CoMMpass cohort (top). Fitted density plot showing mutational scores of driver genes in plasma cells (left-bottom). Violin plots showing the mutational score in MM cell clusters (right-bottom).

(D) Barplot showing enriched pathways in gene modules specific to sub-C4. The analysis was performed by Metascape.

(E) Kaplan-Meier curve showing the overall survival of 414 MM patients with a high or low proportion of sub-C4 in the GSE2658. Log-rank test was applied in the comparison between groups.

(F) Forest plot showing the hazard ratio of 7 genes by univariate Cox regression in MMRF-CoMMpass cohort.

Fig. 4 | The expression pattern of the top one gene LILRB4 in MM cells

(A) Fitted density plots illustrating the expression of 7 specific genes selected by the lasso regression. algorithm in plasma cells.

(B) Bar plot showing the expression of LILRB4 in UAMS-7 groups (PR-proliferation, LB-low bone disease, MS-MMSET, HY-hyperdiploid, MF-MAF/MAFB, CD1/ CD2-CCND1/CCND3).

(C) Bar plot illustrating the LILRB4 expression in healthy individual (HD), monoclonal gammopathy of undetermined significance (MGUS), smoldering multiple myeloma (SMM), and multiple myeloma (MM) patients.

(D) Kaplan-Meier curve showing the overall survival of newly diagnosed (NDMM) patients (left panel, GSE2658) and relapsed/refractory MM (RRMM) patients (right panel, GSE57317) with high or low expression of LILRB4. Log-rank test was applied in the comparison between groups.

(E) Density dot plots and line charts (upper panel) of flow cytometry analysis displaying the expression of LILRB4 protein in the population of plasma cells (PC), malignant plasma cells (MPC), pre-PCs, and normal plasma cells (NPC) from bone marrow aspirates of NDMM and RRMM patients. Bar plots showing the statistical result between different plasma-cell populations. Unpaired *t*-test, ***P<0.001.

(F) (Left) Bar plot showing the flow cytometry detection of LILRB4 in MM cells in NDMM (n=49), post-treatment MM patients (n=31), and RRMM patients (n=12). (Right) Dot plot showing the mRNA expression of LILRB4 in NDMM and RRMM patients. Unpaired *t*-test, *P<0.05, ****P<0.0001.

(G) Density dot plots of flow cytometry analysis displaying LILRB4^{+} and LILRB4^{-} MM cells. Optical microscope image showing the colony formation assay of LILRB4^{+} and LILRB4^{-} cells (5X magnification). Unpaired *t*-test, *P<0.05, **P<0.01.

Fig. 5 | LILRB4 played faceted roles in MM progression

(A) (Left) Flow cytometry detection of LILRB4 in (non-target) NT and LILRB4 knock-out (KO) MM cells. (Right) Growth of LILRB4-KO cells relative to NT multiple myeloma (MM) cells.

(B) Colony formation assay of LILRB4-KO cells relative to NT MM cells (5X magnification).

(C) Transwell invasion assay of LILRB4-KO cells relative to NT MM cells.

(D) Cellular apoptosis detection of NT cells and LILRB4-KO MM cells.

(E) Bar plot showing cytotoxicity towards NT cells and LILRB4-KO MM cells by carfilzomib at 48h.

(F) The H929-NT and H929-KO cells were injected subcutaneously into the left and right flank of the same mouse. Line plot showing the measurement of tumor volume every other day between H929-NT and H929-KO groups. Bar plots showing the statistical result of tumor weight between H929-NT and H929-KO group. Unpaired *t* test, **P*<0.05, ***P*<0.01, ****P*<0.001, *****P*<0.0001.

Fig. 6 | The regulated mechanisms underlying LILRB4 expression in MM cells

(A) ATAC-seq unveiling significant increase in chromatin accessibility within the promoter region of LILRB4 gene in multiple myeloma (MM) cell lines exhibiting elevated expression levels of LILRB4.

(B) STAT1 ChIP-seq reads enriched in the *LILRB4* promoter region.

(C) *LILRB4* mRNA expression in MM cells treated by STAT1 inhibitor, fludarabine, for 48h.

(D) Schematic diagram showing experimental process that MM cells cocultured with healthy peripheral blood mononuclear cells (PBMCs) for 72h. Bar plots showing *LILRB4* mRNA expression and LILRB4 mean fluorescence intensity (MFI) in MM cells respectively after co-culture. Histogram showing flow cytometry examination of LILRB4 in MM cells after co-culture.

Fig. 7 | High infiltrated immunosuppressive myeloid cells in EM24 MM patients

(A) T-distributed stochastic neighbor embedding (tSNE) plots showing the distribution of annotated myeloid cells. Cell annotations are labeled by colors.

(B) TSNE plots showing the marker gene expression of each cell cluster.

(C) Point plot displaying changes in myeloid cell composition between patients with early death (EM24) and patients without early death (nEM24). For each cell type, two axes indicate the log fold change in mean cell fraction between the two groups, with -log10 two-side Wilcoxon rank sum *P*-value.

(D) Scatterplots showing DC migratory and activated scores (left-top), pro- and anti-inflammatory scores (right-top), M1 and M2 polarization scores (left-bottom), and immune activation and suppression scores (right-bottom) for colored myeloid cell types. Triangles represent the median of cell score.

(E) Schematic diagram showing experimental process. Multiple myeloma (MM) cells were co-cultured with peripheral blood mononuclear cells (PBMCs) from healthy donors (HDs), followed by the detection of myeloid-derived suppressive cells (MDSCs) differentiation and T-cell proportion. Bar plots showing the proportion of MDSCs and $CD3^+$ T cells in PBMCs after co-culturing with H929 MM cells with different LILRB4 levels, respectively with unpaired Student's t-test, two-tailed, *P<0.05, ****P<0.0001.

(F) (Left panel) Schematic diagram of experimental process. The non-target (NT) and LILRB4 knock-out (KO) H929 cells were injected subcutaneously into the mice, followed by detection of infiltrated MDSCs in tumor samples. Density dot plots displaying MDSCs population in two groups (left-bottom). Bar plots (right panel) showing the MDSCs proportion in myeloid cells between NT and LILRB4-KO group with unpaired Student's t-test, two-tailed, *P<0.05.

Fig. 8 | LILRB4 is a promising target for immunotherapy of MM

(A) Density dot plots of flow cytometry analysis displaying the expression of LILRB4 protein in the population of monocytic myeloid-derived suppressive cells (M-MDSC) and granulocytic myeloid-derived suppressive cells (G-MDSC) from multiple myeloma (MM) patients. Strategies for gating are shown in the figure. Bar plot showing the expression of LILRB4 protein in M-MDSC and G-MDSC (bottom-right).

(B) Density line charts (top panel) of flow cytometry analysis displaying the expression of LILRB4 protein in NCI-H929 and U266 multiple myeloma (MM) cells. Points plot showing cell lysis percentage of NCI-H929 and U266 MM cells co-cultured with mock-T cells (yellow) or LILRB4-targeted synthetic T cell receptor and antigen receptor (STAR)-T cells (purple) under different effector: target (E: T) ratio and different incubating time (middle panel). Bar plots showing the concentration of IFN-γ, IL-2, and TNF-α secreted by T cells after co-culture (bottom panel).

(C) (Left) Schematic of the monitoring of the anti-tumor function of LILRB4 STAR-T cells in a xenograft tumor model. (Middle) Line charts illustrating the subcutaneous tumor volume in MM xenograft mice after treating mock-T cells or LILRB4-targeted STAR-T cells. The mean tumor volumes with standard error bars were calculated on specific days. (Right) Kaplan-Meier curve showing the survival of MM xenograft mice.

(D) Density line charts of flow cytometry analysis displaying the expression of LILRB4 protein in monocyte-derived MDSCs. Bar plots showing the cell lysis percentage of monocyte-derived MDSCs co-cultured with mock-T cells or LILRB4-targeted STAR-T cells (left panel). Bar plots showing the concentration of IFN-γ, IL-2, and TNF-α after co-culture (right panel).

(E) Exemplary dot plots obtained in the flow cytometry-based LILRB4 STAR-T cell cytotoxicity assay. Bone marrow mononuclear cells (BMMCs) from MM patients (n=9) were cocultured with LILRB4 STAR-T or mock-transduced T cells at different E: T ratios. After 4 hours of incubation, specific lysis of $CD38^{+}LILRB4^{+}$ cells and $CD11b^{+}LILRB4^{+}$ immunosuppressive myeloid cells by LILRB4 STAR-T or mock-transduced T cells were quantified and calculated by flow cytometry using counting beads.

Fig. 1

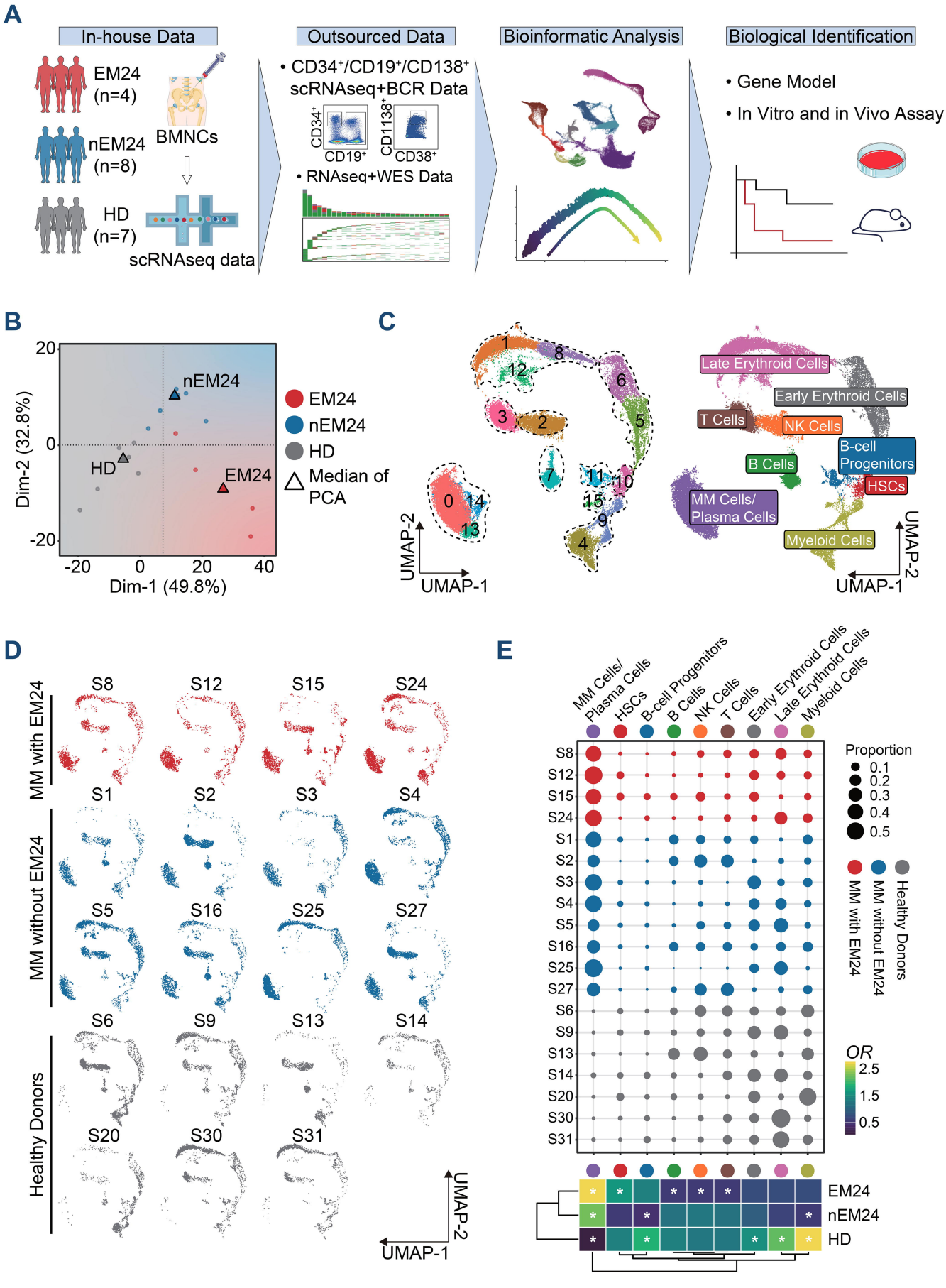
A
In-house Data
EM24 (n=4)
nEM24 (n=8)
HD (n=7)
BMNCs
scRNAseq data
Outsourced Data
• CD34+/CD19+/CD138+ scRNAseq+BCR Data
CD34+
CD19+
CD1138+
CD38+
• RNAseq+WES Data
Bioinformatic Analysis
Biological Identification
• Gene Model
• In Vitro and in Vivo Assay
B
Dim-2 (32.8%)
Dim-1 (49.8%)
nEM24
HD
EM24
EM24
nEM24
HD
Median of PCA
C
UMAP-2
UMAP-1
Late Erythroid Cells
Early Erythroid Cells
T Cells
NK Cells
B-cell Progenitors
B Cells
HSCs
MM Cells/ Plasma Cells
Myeloid Cells
D
MM with EM24
MM without EM24
Healthy Donors
S8
S12
S15
S24
S1
S2
S3
S4
S5
S16
S25
S27
S6
S9
S13
S14
S20
S30
S31
UMAP-2
UMAP-1
E
MM Cells/ Plasma Cells
HSCs
B-cell Progenitors
B Cells
NK Cells
T Cells
Early Erythroid Cells
Late Erythroid Cells
Myeloid Cells
Proportion
0.1
0.2
0.3
0.4
0.5
MM with EM24
MM without EM24
Healthy Donors
OR
2.5
1.5
0.5
EM24
nEM24
HD

Fig. 2

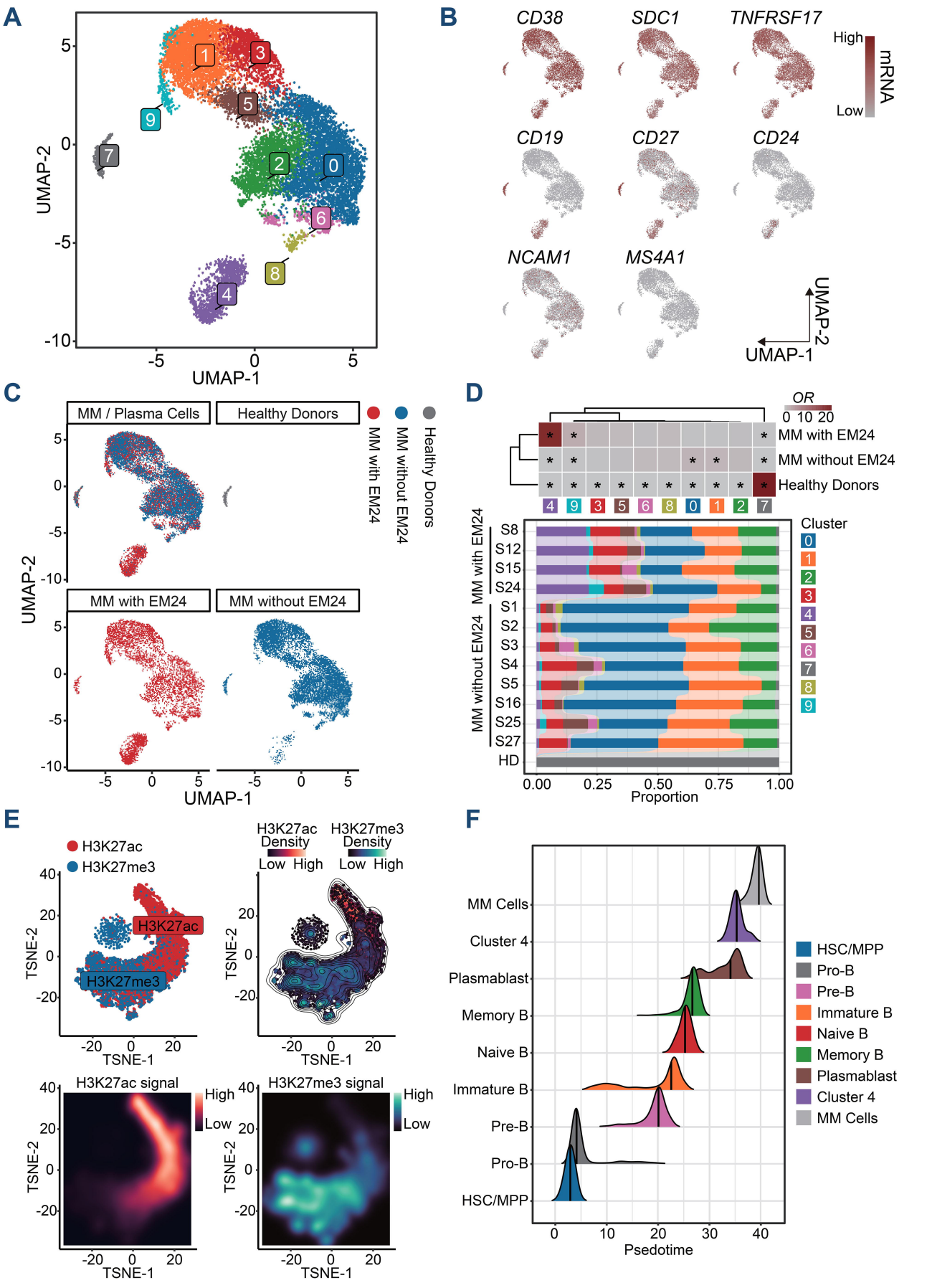
A
UMAP-2
UMAP-1
B
CD38
SDC1
TNFRSF17
CD19
CD27
CD24
NCAM1
MS4A1
High
Low
mRNA
C
MM / Plasma Cells
Healthy Donors
MM with EM24
MM without EM24
MM with EM24
MM without EM24
Healthy Donors
D
OR
0 10 20
MM with EM24
MM without EM24
Healthy Donors
Cluster
MM with EM24
MM without EM24
HD
Proportion
E
H3K27ac
H3K27me3
H3K27ac Density
H3K27me3 Density
Low High
H3K27ac signal
H3K27me3 signal
TSNE-1
TSNE-2
F
MM Cells
Cluster 4
Plasmablast
Memory B
Naive B
Immature B
Pre-B
Pro-B
HSC/MPP
Psedotime
HSC/MPP
Pro-B
Pre-B
Immature B
Naive B
Memory B
Plasmablast
Cluster 4
MM Cells

Fig. 3

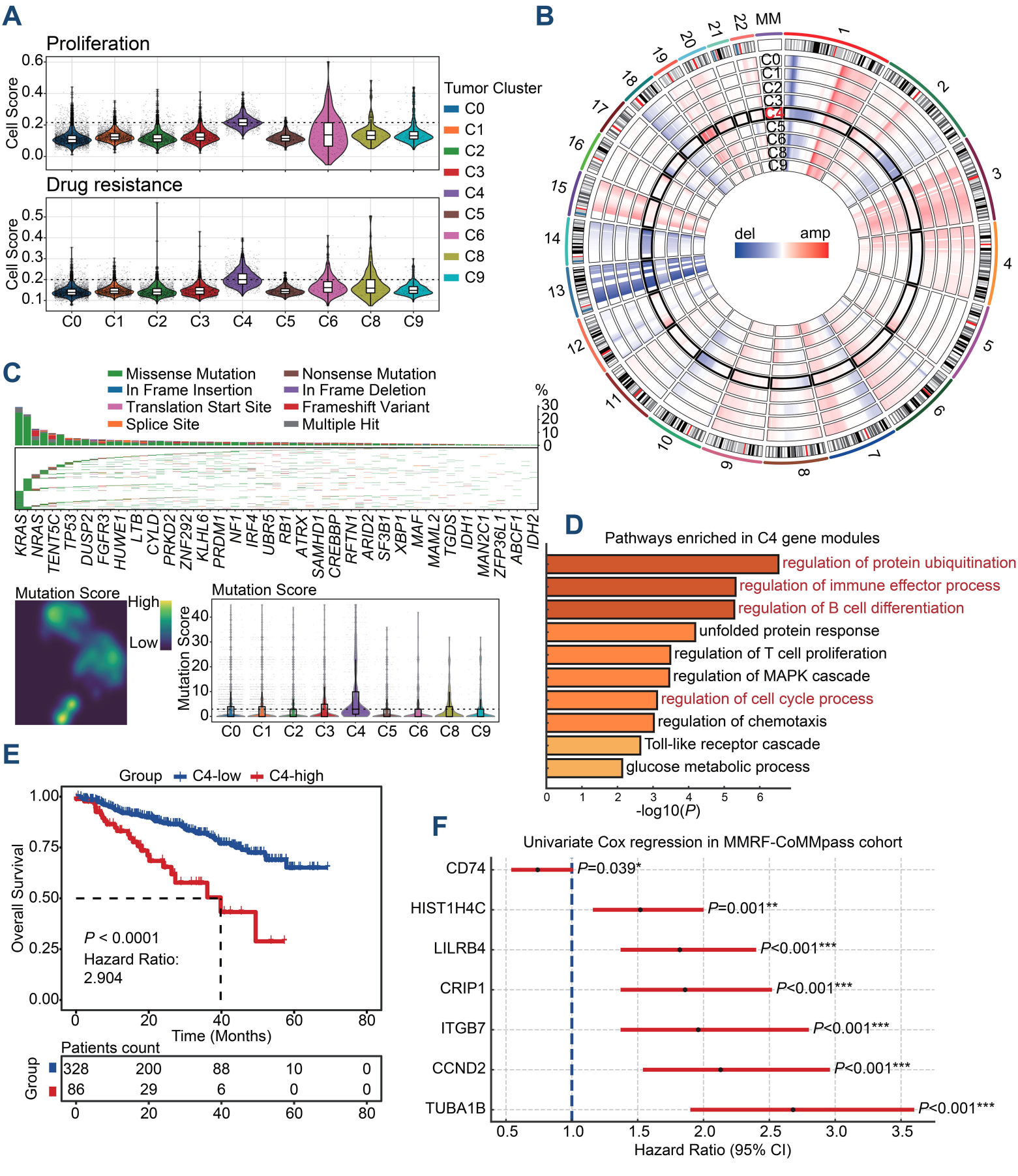
A
Proliferation
Cell Score
Drug resistance
Tumor Cluster
C0
C1
C2
C3
C4
C5
C6
C8
C9
B
MM
del
amp
C
Missense Mutation
Nonsense Mutation
In Frame Insertion
In Frame Deletion
Translation Start Site
Frameshift Variant
Splice Site
Multiple Hit
KRAS NRAS TENT5C TP53 DUSP2 FGFR3 HUWE1 LTB CYLD PRKD2 ZNF292 KLHL6 PRDM1 NF1 IRF4 UBR5 RB1 ATRX SAMHD1 CREBBP RFTN1 ARID2 SF3B1 XBP1 MAF MAML2 TGDS IDH1 MAN2C1 ZFP36L1 ABCF1 IDH2
Mutation Score
High
Low
D
Pathways enriched in C4 gene modules
regulation of protein ubiquitination
regulation of immune effector process
regulation of B cell differentiation
unfolded protein response
regulation of T cell proliferation
regulation of MAPK cascade
regulation of cell cycle process
regulation of chemotaxis
Toll-like receptor cascade
glucose metabolic process
-log10(P)
E
Group C4-low C4-high
Overall Survival
P < 0.0001
Hazard Ratio: 2.904
Time (Months)
Patients count
328 200 88 10 0
86 29 6 0 0
F
Univariate Cox regression in MMRF-CoMMpass cohort
CD74 P=0.039*
HIST1H4C P=0.001**
LILRB4 P<0.001***
CRIP1 P<0.001***
ITGB7 P<0.001***
CCND2 P<0.001***
TUBA1B P<0.001***
Hazard Ratio (95% CI)

Fig. 4

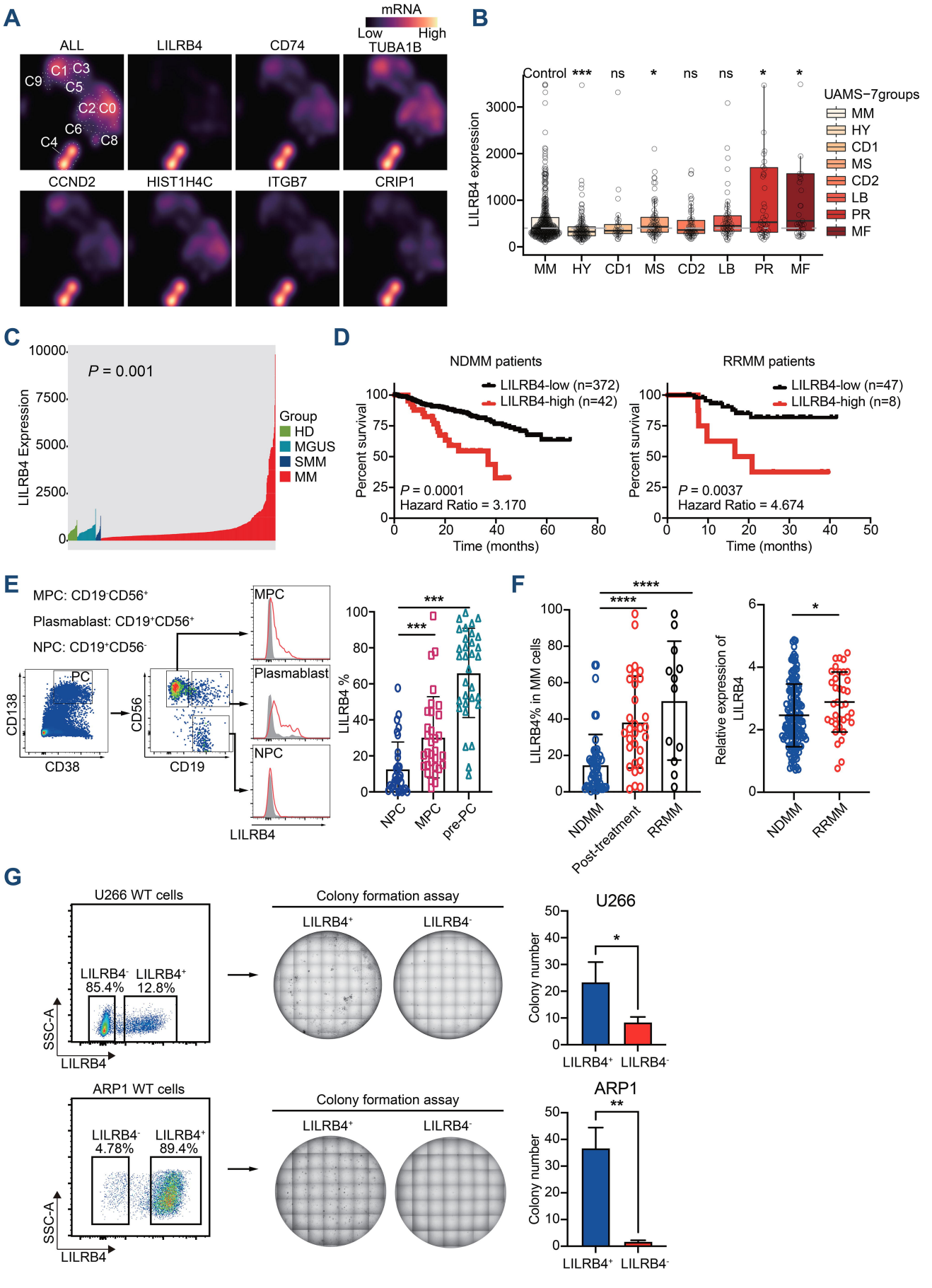
A
mRNA
Low
High
ALL
LILRB4
CD74
TUBA1B
C1
C3
C9
C5
C2
C0
C6
C4
C8
CCND2
HIST1H4C
ITGB7
CRIP1
B
Control
***
ns
*
ns
ns
*
*
LILRB4 expression
3000
2000
1000
0
MM
HY
CD1
MS
CD2
LB
PR
MF
UAMS−7groups
MM
HY
CD1
MS
CD2
LB
PR
MF
C
P = 0.001
LILRB4 Expression
10000
7500
5000
2500
0
Group
HD
MGUS
SMM
MM
D
NDMM patients
LILRB4-low (n=372)
LILRB4-high (n=42)
Percent survival
100
75
50
25
0
P = 0.0001
Hazard Ratio = 3.170
0
20
40
60
80
Time (months)
RRMM patients
LILRB4-low (n=47)
LILRB4-high (n=8)
Percent survival
100
75
50
25
0
P = 0.0037
Hazard Ratio = 4.674
0
10
20
30
40
50
Time (months)
E
MPC: CD19-CD56+
Plasmablast: CD19+CD56+
NPC: CD19+CD56-
PC
CD138
CD38
CD56
CD19
MPC
Plasmablast
NPC
LILRB4
***
***
LILRB4 %
100
80
60
40
20
0
NPC
MPC
pre-PC
F
****
****
LILRB4% in MM cells
100
80
60
40
20
0
NDMM
Post-treatment
RRMM
*
Relative expression of LILRB4
6
4
2
0
NDMM
RRMM
G
U266 WT cells
LILRB4-
85.4%
LILRB4+
12.8%
SSC-A
LILRB4
Colony formation assay
LILRB4+
LILRB4-
U266
*
Colony number
50
40
30
20
10
0
LILRB4+
LILRB4-
ARP1 WT cells
LILRB4-
4.78%
LILRB4+
89.4%
SSC-A
LILRB4
Colony formation assay
LILRB4+
LILRB4-
ARP1
**
Colony number
50
40
30
20
10
0
LILRB4+
LILRB4-

Fig. 5

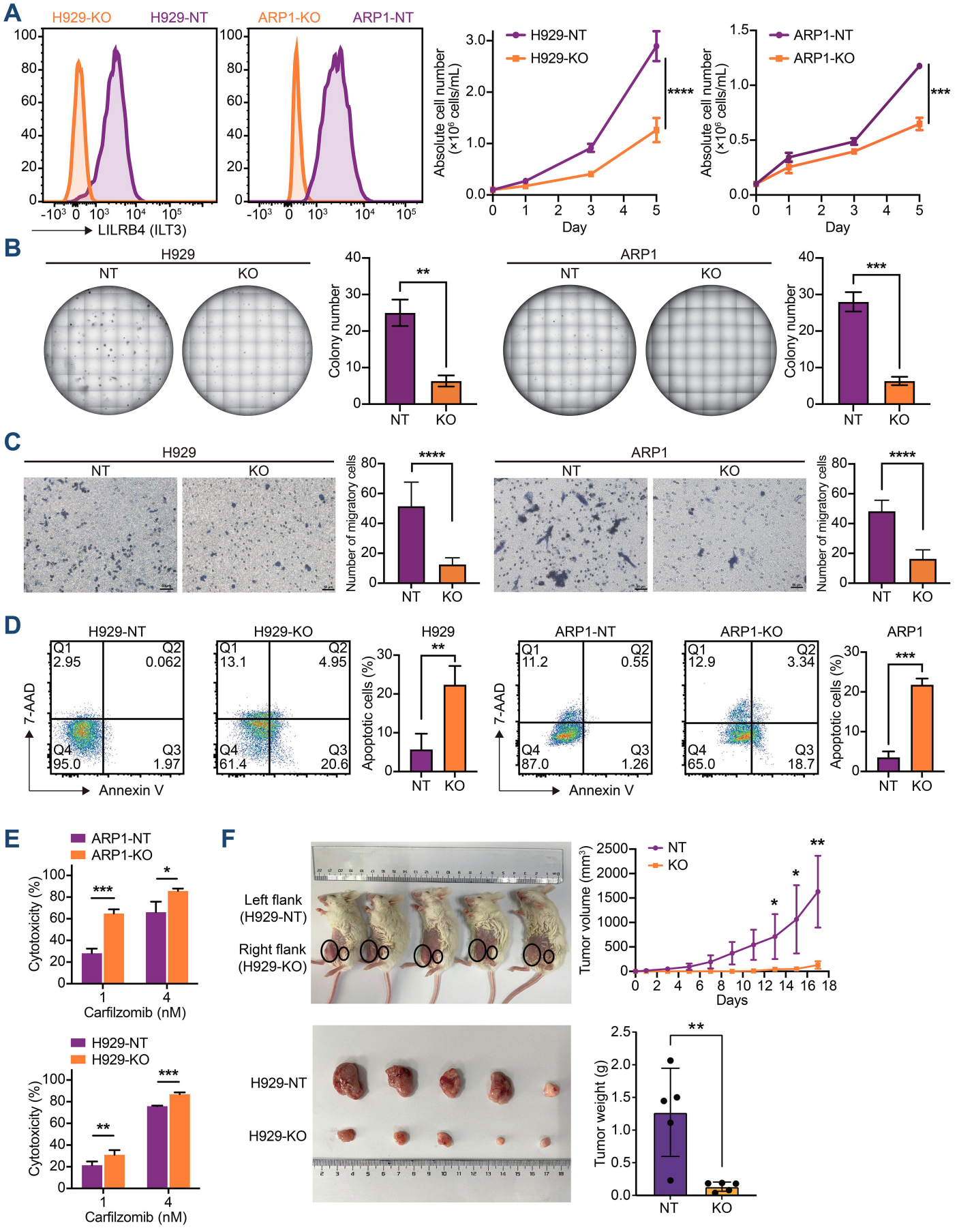
A
H929-KO
H929-NT
ARP1-KO
ARP1-NT
LILRB4 (ILT3)
Absolute cell number (×10⁶ cells/mL)
Day
B
H929
ARP1
NT
KO
Colony number
C
Number of migratory cells
D
Q1
Q2
Q3
Q4
7-AAD
Annexin V
Apoptotic cells (%)
E
Cytotoxicity (%)
Carfilzomib (nM)
F
Left flank (H929-NT)
Right flank (H929-KO)
Tumor volume (mm³)
Days
Tumor weight (g)

Fig. 6

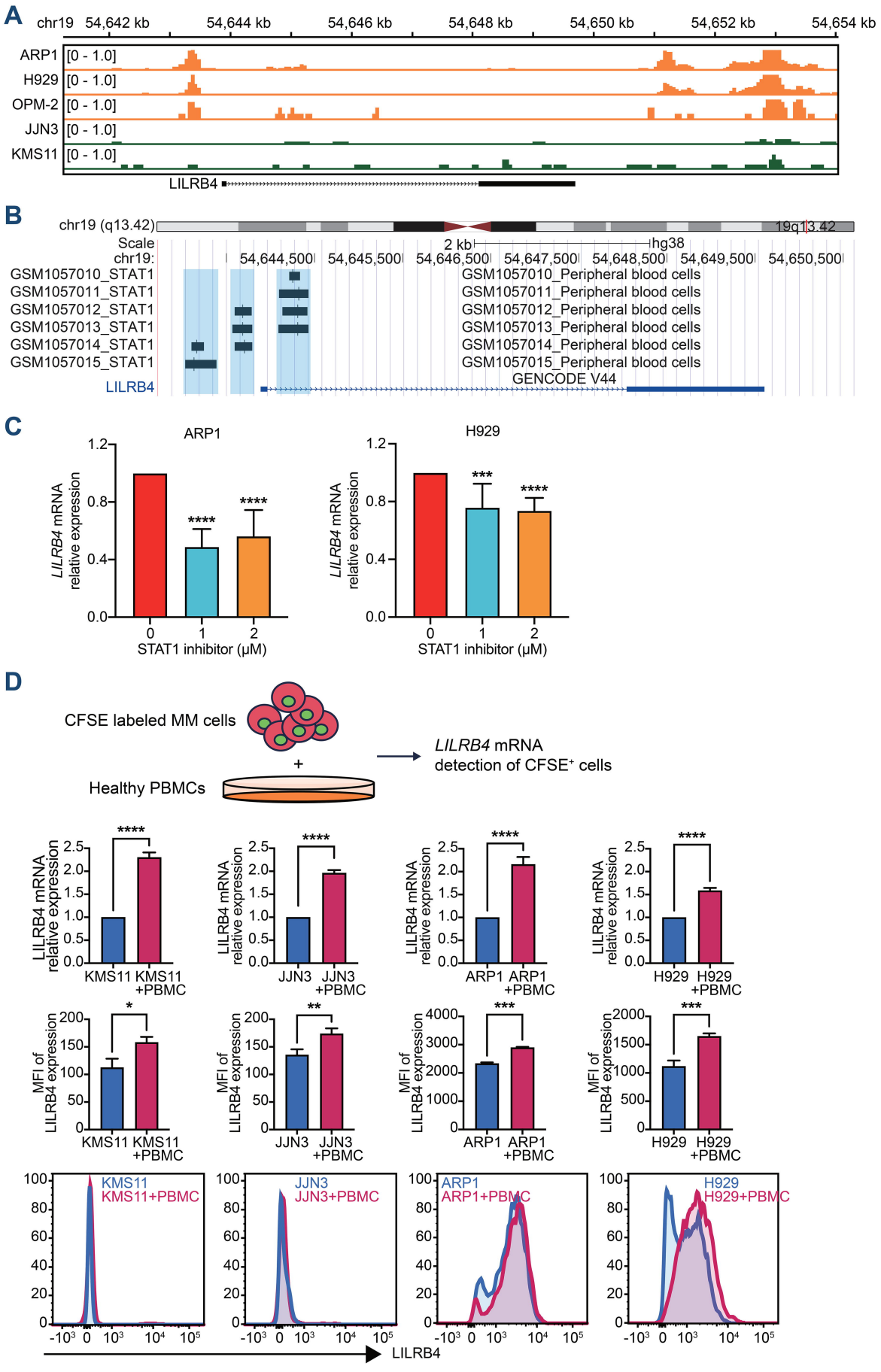
A
chr19 54,642 kb
54,644 kb
54,646 kb
54,648 kb
54,650 kb
54,652 kb
54,654 kb
ARP1 [0 - 1.0]
H929 [0 - 1.0]
OPM-2 [0 - 1.0]
JJN3 [0 - 1.0]
KMS11 [0 - 1.0]
LILRB4
B
chr19 (q13.42)
19q13.42
Scale
2 kb
hg38
chr19:
54,644,500
54,645,500
54,646,500
54,647,500
54,648,500
54,649,500
54,650,500
GSM1057010_STAT1
GSM1057011_STAT1
GSM1057012_STAT1
GSM1057013_STAT1
GSM1057014_STAT1
GSM1057015_STAT1
GSM1057010_Peripheral blood cells
GSM1057011_Peripheral blood cells
GSM1057012_Peripheral blood cells
GSM1057013_Peripheral blood cells
GSM1057014_Peripheral blood cells
GSM1057015_Peripheral blood cells
GENCODE V44
LILRB4
C
ARP1
H929
LILRB4 mRNA relative expression
STAT1 inhibitor (μM)
D
CFSE labeled MM cells
+
Healthy PBMCs
LILRB4 mRNA detection of CFSE+ cells
LILRB4 mRNA relative expression
MFI of LILRB4 expression
KMS11
KMS11 +PBMC
JJN3
JJN3 +PBMC
ARP1
ARP1 +PBMC
H929
H929 +PBMC
KMS11+PBMC
JJN3+PBMC
ARP1+PBMC
H929+PBMC
LILRB4

Fig. 7

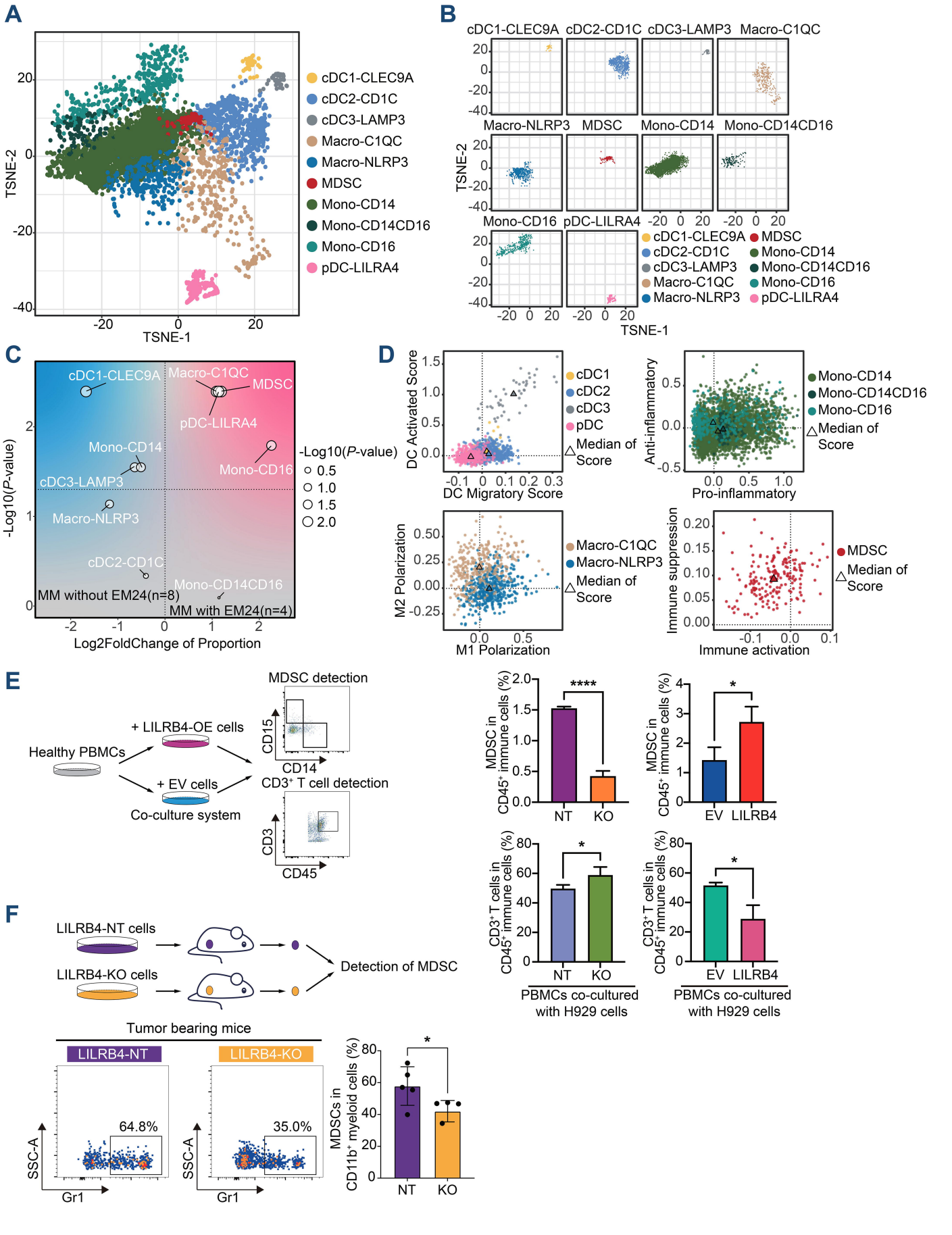
A
TSNE-1
TSNE-2
cDC1-CLEC9A
cDC2-CD1C
cDC3-LAMP3
Macro-C1QC
Macro-NLRP3
MDSC
Mono-CD14
Mono-CD14CD16
Mono-CD16
pDC-LILRA4
B
cDC1-CLEC9A
cDC2-CD1C
cDC3-LAMP3
Macro-C1QC
Macro-NLRP3
MDSC
Mono-CD14
Mono-CD14CD16
Mono-CD16
pDC-LILRA4
TSNE-1
TSNE-2
C
-Log10(P-value)
Log2FoldChange of Proportion
MM without EM24(n=8)
MM with EM24(n=4)
D
DC Activated Score
DC Migratory Score
cDC1
cDC2
cDC3
pDC
Median of Score
Anti-inflammatory
Pro-inflammatory
M2 Polarization
M1 Polarization
Immune suppression
Immune activation
E
MDSC detection
+ LILRB4-OE cells
Healthy PBMCs
+ EV cells
Co-culture system
CD3+ T cell detection
MDSC in CD45+ immune cells (%)
CD3+T cells in CD45+ immune cells (%)
NT
KO
EV
LILRB4
PBMCs co-cultured with H929 cells
F
LILRB4-NT cells
LILRB4-KO cells
Detection of MDSC
Tumor bearing mice
64.8%
35.0%
SSC-A
Gr1
MDSCs in CD11b+ myeloid cells (%)

Fig. 8

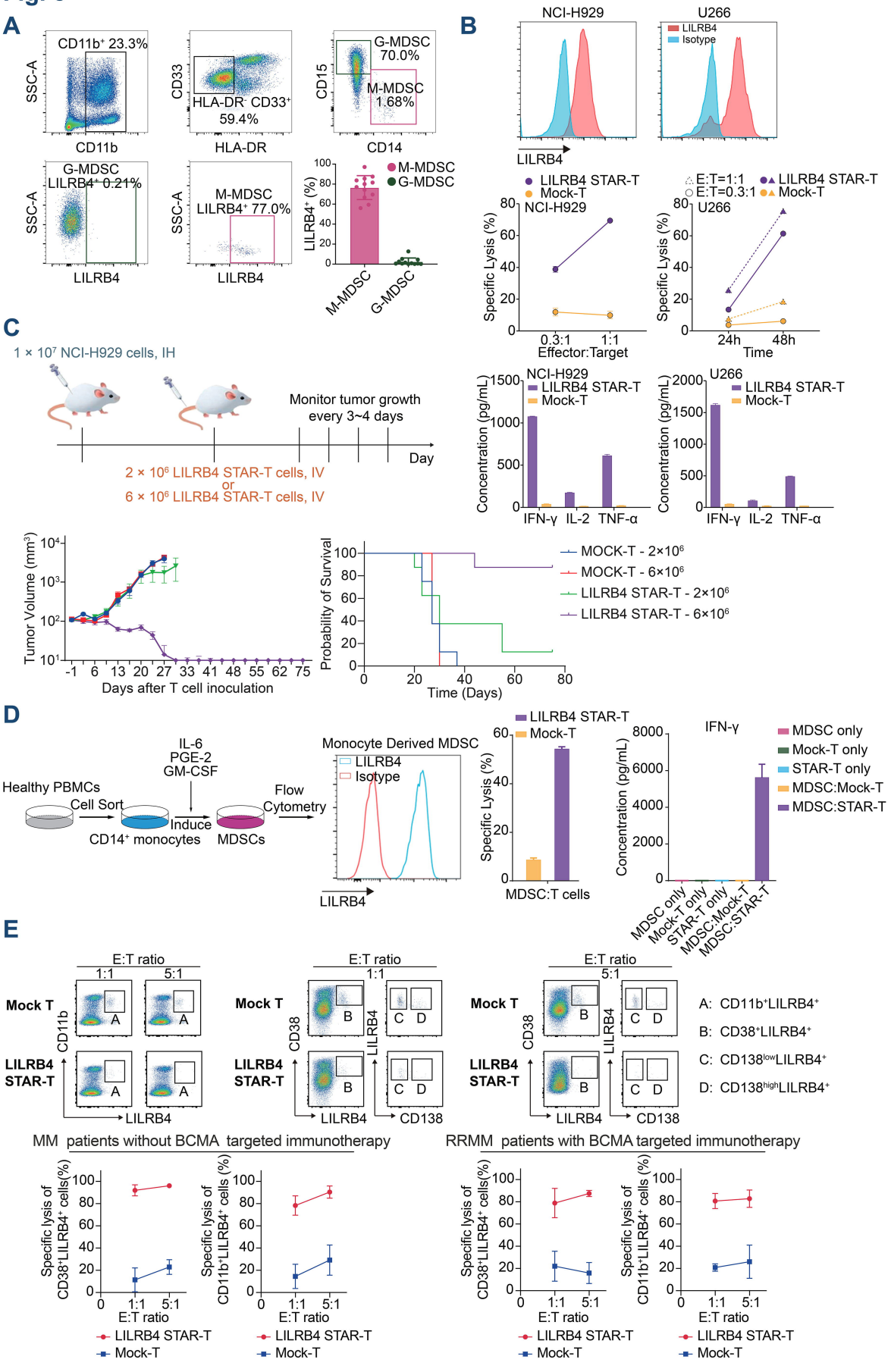
A
CD11b+ 23.3%
SSC-A
CD11b
CD33
HLA-DR- CD33+
59.4%
HLA-DR
CD15
G-MDSC
70.0%
M-MDSC
1.68%
CD14
G-MDSC
LILRB4+ 0.21%
LILRB4
M-MDSC
LILRB4+ 77.0%
LILRB4+ (%)
M-MDSC
G-MDSC
B
NCI-H929
U266
LILRB4
Isotype
LILRB4
LILRB4 STAR-T
Mock-T
Specific Lysis (%)
Effector:Target
E:T=1:1
E:T=0.3:1
Time
24h
48h
Concentration (pg/mL)
IFN-γ
IL-2
TNF-α
C
1 × 10⁷ NCI-H929 cells, IH
Monitor tumor growth
every 3~4 days
Day
2 × 10⁶ LILRB4 STAR-T cells, IV
or
6 × 10⁶ LILRB4 STAR-T cells, IV
Tumor Volume (mm³)
Days after T cell inoculation
Probability of Survival
Time (Days)
MOCK-T - 2×10⁶
MOCK-T - 6×10⁶
LILRB4 STAR-T - 2×10⁶
LILRB4 STAR-T - 6×10⁶
D
Healthy PBMCs
Cell Sort
CD14+ monocytes
IL-6
PGE-2
GM-CSF
Induce
MDSCs
Flow
Cytometry
Monocyte Derived MDSC
LILRB4
Isotype
MDSC:T cells
MDSC only
Mock-T only
STAR-T only
MDSC:Mock-T
MDSC:STAR-T
E
E:T ratio
1:1
5:1
Mock T
LILRB4 STAR-T
CD11b
CD38
CD138
A: CD11b+LILRB4+
B: CD38+LILRB4+
C: CD138low LILRB4+
D: CD138high LILRB4+
MM patients without BCMA targeted immunotherapy
RRMM patients with BCMA targeted immunotherapy
Specific lysis of CD38+LILRB4+ cells(%)
Specific lysis of CD11b+LILRB4+ cells (%)

Supplemental files

Methods

Sample collection and single cell preparation

BMMCs were isolated by Ficoll (MERCK) density-gradient centrifugation and cryopreserved at -80°C for less than five days until processed. The number and viability of cells was measured using a TC20 automated cell counter (Biorad). Dead cells (cell viability less than 80%) were removed by magnetic bead purification (Miltenyi Biotech) according to the manufacturer's protocol before scRNA-seq.

Single-cell RNA library preparation and sequencing

Chromium single-cell sequencing technology was performed following the manufacturer's protocol (10× Genomics). Library construction procedures were performed using the Chromium Single Cell 3' Library, Gel Bead & Multiplex Kit (10× Genomics, V2), strictly following the manufacturer's instructions. Then the cell suspensions were loaded onto the 10x Chromium Single Cell Controller to generate single-cell gel bead-in-emulsions (GEMs), and we performed barcoded reverse transcription of RNA within a single cell using a Verity Thermal Cycler (Life Technologies). Through reverse transcription in a single GEM, the barcodes were added to the RNAs released from lysed cells; then fragmentation, end repair, polyA tailing, and adaptor ligation were achieved according to the standard protocol. The cDNA purification and size selection were performed by SPRI select beads (Beckman Coulter), and the quality was evaluated using the Agilent Bioanalyzer. Finally, the libraries were sequenced on an MGISEQ-2000 sequencer as 150 bp paired-end reads by Beijing Genomics Institute (BGI, Shenzhen, China).

scRNA-seq data processing

The Cell Ranger Software Suite (version 3.0.2; 10x Genomics) was used to perform sample de-multiplexing, alignment, barcode processing, and unique molecular identifier (UMI) counting. Briefly, sequencing reads were aligned against the GRCh38 human reference genome with STAR, and count matrices were built from the resulting BAM files.(1) The R package scCancer v2.1.0(2) was then used to conduct the quality control, which detected outliers automatically according to the distributions of the metrics. First, the number of total unique molecular identifiers (UMI; nUMI), number of expressed genes (nGene), and percentage of UMIs from mitochondrial genes (mito.percent), ribosomal genes (ribo.percent) and dissociation-associated genes (diss.percent) were used to filter low-quality cells and multiplets (see the auto-selected thresholds in **Suppl. Fig. 1B**). We then filtered the genes that were expressed in <3 cells. For the integration of the cells from different samples, we corrected batch effect using the R package

harmony (version 0.1.1).(3) In parameter settings, the first 30 dimensions of canonical correlation analysis (CCA) and principal component analysis (PCA) were used.

Dimensionality reduction, clustering of cells, and visualization

The R package Seurat v.3 was used for data scaling, transformation, clustering, dimensionality reduction, differential expression analysis, and most visualizations.(4, 5) The variable genes were identified using the 'vst' method in the Seurat 'FindVariableFeatures' function. PCA was performed using the top 2,000 variable genes. Graph-based clustering was performed on the PCA-reduced data for clustering analysis. The resolution was set to 0.5 to obtain a more refined result. Briefly, the first 50 PCs of the integrated gene-cell matrix were used to construct a shared nearest-neighbor graph (SNN; 'FindNeighbors'), and this SNN was used to cluster the dataset ('FindClusters') using a graph-based modularity-optimization algorithm of the Louvain method for community detection. Then UMAP was performed on the top 30 principal components for visualizing the cells.

Cell cluster annotation with specific maker genes expression

The marker genes, identified by the 'FindAllMarkers' function—with the setting 'only.pos' as 'True', 'min.pct' as 0.25, 'logfc.threshold' as 0.25 and 'test.use' as 'wilcox'—were used to annotate cell clusters. Cluster annotation was confirmed using the celltypist, an automated cell type annotation tool for scRNA-seq datasets based on logistic regression classifiers optimised by the stochastic gradient descent algorithm.(6)

Characterizing the cell distribution in sample groups

To characterize the group distribution of cells, odds ratios (OR) were calculated and used to indicate preferences as reported.(7) Specifically, for each combination of cells i and group j, a 2 by 2 contingency table was constructed, which contained the number of cells i in group j, the number of cells of cell i in other groups, the number of non-i cells in group j, the number of non-i cells in other groups. Then Fisher's exact test was applied on this contingency table, thus OR and corresponding p-value could be obtained. We labeled groups with a p-value < 0.05 using an asterisk (*). A higher OR with an asterisk indicated that cells i was more preferred to distribute in group j, while a lower OR with an asterisk indicated that cells i was preferred to less distribute in group j.

Plasma-cell lineage developmental trajectory

The scRNA-seq data of $CD34^+$, $CD19^+$, and $CD138^+$ cells from healthy donors including PRJCA003794(8) and PRJNA732205(9) were used to build the plasma-cell lineage and differentiation stage classifier. Pseudotime-ordered analysis of HSCs, pro-B cells, pre-B cells, immature B cells, naïve B cells, memory

B cells, plasmablasts, and plasma cells was performed using Monocle2.(10)

Plasma-cell differentiation stage classifier

To discriminate the differentiation stage of MM cell clusters, we trained a plasma-cell differentiation stage classifier using random forest training. The training was based on eight annotated cells representing different differentiation stages (HSCs, pro-B cells, pre-B cells, immature B cells, naïve B cells, memory B cells, plasmablasts, and plasma cells). We utilized the 'FindAllMarkers' function from Seurat v.3 to select the top 100 marker genes for each stage, sorted according to the average fold change. Cell cycle-related genes, mitochondrial genes, ribosomal genes, and genes associated with cell dissolution were removed, resulting in 597 non-redundant feature genes in total. The normalized gene-cell matrix by Seurat v.3 was randomly split into a 70% training set and a 30% validation set using the caTools package. The training was performed using the 'randomForest' function from the randomForest v4.6 package, generating 500 trees. For testing, we used the 'roc' function from the pROC package v1.18.0 to calculate the sensitivity and specificity of the predictions for each cell type in the validation set. Finally, we utilized ggroc v1.0 to plot the ROC curves.

Processing of scBCR-seq data

The outsourced scBCR-seq were processed using CellRanger v3.0.2 (‘vdj’ pipeline with default setting and using the V(D)J library GRCh38) and the output files with cell and clonotype information were generated. According to the clonotypes provided by the file ‘filtered_contig_annotations.csv’, we counted the cell number of each clonotype as its abundance. Cells were assigned to ‘abundance>10′, ‘abundance≤10’ or ‘none’ according to the abundance of their clonotypes.

Calculating the proportion of Kappa$^+$ cells

The human genome has one kappa constant (IGKC) gene but variable number of lambda constants – IGLC1, IGLC2, IGLC3 and IGLC7 are functional isotypes. Let *t* be a chosen transcript count threshold and *K* the number of cells expressing at least t IGKC transcripts. Further let *L* be the number of cells expressing at least t transcripts of any of three out of the four functional lambda isotypes: IGLC2, IGLC3 and IGLC7.(11) The IGLC1 transcript was not detected in any B cell, probably because complete overlap of its 3’end with the IGLL5 gene precludes IGLC1 mRNA quantification with 3’end RNA-Seq assays. The % kappa$^+$ cells within a given population was calculated as: $Kappa^+ = \frac{K}{K+L}$. t = 1 was chosen. The estimated % of kappa$^+$ cells was robust to different values of *t* ranging between 1 and 5.

Topology of sequenced genes in MM cells

We transposed the gene-by-cell matrix of MM cells and applied dimensionality reduction and clustering techniques to analyze 20,711 genes across 12,835 MM cells using Seurat v.3. To identify genes with differential expression in specific clusters or samples, we employed the 'FindMarkers' function with the 'wilcox' parameter, conducting the Wilcoxon rank-sum test with a significance threshold of $P<0.05$. Differential genes with a fold change greater than 1 were considered specific to clusters or samples. We utilized UMAP for visualizing their distribution characteristics.

Construction of transcriptional regulatory network and gene co-expression network

We selected specific genes from cluster 4 to infer the transcriptional regulatory network and establish a co-expression network. Candidate transcription factors and transcription factor-target pairs were obtained from TRRUST v2(12), which includes 8,444 regulatory interactions (annotated as ‘activation’, ‘repression’, and ‘unknown’) for 800 transcription factors in humans. We retained only the edges where both the transcription factor and target were present in the specific genes of cluster 4. Moreover, we kept only the transcription factors with at least two edges annotated as ‘activation’ or ‘repression’ in the final network.

To construct the co-expression network, we calculated the Pearson correlation between the specific genes of cluster 4 in cluster 4 MM cells. Genes with a P-value < 0.05 and an absolute correlation coefficient > 0.4 were retained. Clustering of the co-expression network was performed using MCODE in Cytoscape v3.9.0, and the top 4 clusters with a degree cutoff of 5 were kept. The networks were visualized using Gephi v0.10.1 with the ‘Fruchterman Reingold’ layout.

WES data processing and mutation calling from scRNA-seq data

Mutations of reported driver genes(13) were identified from bulk Whole Exome Sequencing (WES) data from 947 newly diagnosed MM patients of MMRF-CoMMpass cohort processed by MuTect2 of GATK pipeline (vcf files of IA20 version, https://tcga-data.nci.nih.gov/). Next, the identified variants were further examined in the scRNA-seq data of the MM cells using cb_sniffer v1.0 (https://github.com/sridnona/cb_sniffer). For this analysis, two additional files generated by CellRanger were required: the aligned BAM file of scRNA-seq data and the corresponding cell barcode file. The output file of cb sniffer with the suffix name ‘counts_CB.tsv’ recorded cell barcodes that had the specific mutation. Finally, the frequency of 63 driver genes mutation in single cell was calculated as mutation score.

The significance of cluster 4 on overall survival of MM patients

Deconvolution of subclusters in bulk tumor cells from GSE2658 RNA martrix was performed using support

vector machine (SVM) algorithms by CIBERSORTx(14). Normalized average expression matrix of 10 plasma cell clusters served as the input signature matrix and the relative cell fraction was further imputed with scRNA-seq mode. The optimal cut point for the fraction of cluster 4 in MM patients was determined using the maximally selected rank statistics from the maxstat R package. The log-rank test was employed to calculate *P*-values between MM patients with high or low cluster 4 fractions, and the Kaplan–Meier method was performed to plot survival curves for survival analyses.

Single cell copy number variations (CNVs) calling

To identify clonal large-scale chromosomal CNVs in malignant MM cells, we used the inferCNV R package to infer the genetic profiles of each cell based on the average expression of large genes sets (101 genes) in each chromosomal region of the tumor genome compared to normal cells(15) All malignant plasma cells MM were input as interrogation group and normal plasma cells from HDs were sampled as control. Other parameters were set as default. CNVs on autosomes were visualized using the R package RCircos(16).

Projection and analysis of myeloid cells

We leveraged STACAS package to integrate pan-cancer myeloid cells from 45 human samples of PRJNA647394 and myeloid-derived suppressor cells (MDSCs) from PRJNA578550 and further built a customized reference atlas for myeloid cells.(17-19) We projected our myeloid cell to this reference map with ProjecTILs v3.1, allowing accurate embedding of new scRNA-seq data into a reference.(20) Subsequently, we calculated MDSC signature, activated score and migratory score of DC cells, anti-/pro-inflammatory score of monocytes, and M1/M2 polarization score of macrophages with reported gene set by AddModuleScore function in Seurat v.3.(18, 19, 21)

RNA sequencing and data processing

Bulk RNA-seq was used to characterize the in-house data of the MM patients for verification. 133 newly diagnosed MM patients were involved at the Institute of Hematology and Blood Diseases Hospital, Chinese Academy of Medical Sciences, and Peking Union Medical College. RNA extraction was performed using the miRNeasy Mini Kit (Qiagen). The RNA yield and cDNA libraries from CD138-selected plasma cells were sequenced on the NextSeq500 Sequencing System (Illumina) with read length of paired-end 150 bp. Raw reads were pre-processed using FastQC software. Clean reads were then used for subsequent analyses. RNA-seq reads were aligned to GRCh38 using STAR. Transcript expression levels were quantified after normalizing the count data with the edgeR package.(22)

ATAC-seq analysis

Assay for Transposase Accessible Chromatin with high-throughput sequencing (ATAC-seq) uses Tn5 transposase to insert adaptors into the accessible region on the genome. The obtained library can directly identify the transcription factor binding region and nucleosome position, providing an effective approach for researching gene regulation and genomic imprinting. ATAC-seq unveiled significant increase in chromatin accessibility within the promoter region of the LILRB4 gene in cell lines exhibiting elevated expression levels of LILRB4.

Cell Culture and transfection

MM cell lines were kept in our laboratory and authenticated by short-tandem repeat (STR) profiling. The MM cell lines with stable LILRB4 overexpression (OE) or deletion (KO) were produced by lentivirus transfection containing LILRB4-OE plasmid (pCDH-EF1A-h*LILRB4*-T2A-Puro) or Cas9-expressing plasmids containing guide RNA (LentiCRISPR v2) respectively. The guide RNA sequences used for LILRB4 were listed in **Table S4**. Lentivirus packaging, the constructs for gene overexpression and CRISPR-Cas9-based constructs were performed according to our previous study.(23, 24) For LILRB4 knock-out, LILRB4 or control CRISPR lentivirus were transduced into cells and sorted via FACS isolation. Single clones were selected and validated by flow detection.

Colony-formation assay

A total of 1 000 MM cells were plated in triplicate in 1.1 ml methylcellulose-based medium (MethoCult™ H4230, StemCell Technologies) per 12-well and incubated for 2 weeks. The culture plate was taken photo under high-content analysis system (Operetta CLS). Colonies consisting of more than 50 cells were scored.

Co-culture assay

For MDSC induction, MM cells (1×10^5) and PBMCs from healthy donors (1×10^6) were co-cultured in 10% RPMI 1640 for 6 days. MDSC detection ($CD11b^+CD33^+HLA\text{-}DR^{-/low}$) was performed by flow cytometry analysis. The in vitro experiments were performed in triplicate and repeated three times.

For examining the regulation of LILRB4 expression by microenvironment cells, MM cells were firstly labeled by CFSE. Then MM cells and PBMCs from healthy donors were co-cultured at the ratio of 1:10. After 3-day coculture, LILRB4 expression in $CFSE^+$ MM cells was examined by flow cytometry. At the same time, $CFSE^+$ MM cells were sorted by flow cytometry for *LILRB4* mRNA detection.

MDSC generation

For MDSC cytotoxicity assay, MDSCs were induced in vitro. $CD14^+$ monocytes were isolated from HD PBMCs following the EasySep Human Monocyte Isolation Kit (Stem cell, 19359). After isolation, monocytes were cultured in RPMI 1640 complete medium with the addition of IL-6 (10ng/ml) & GM-CSF (10ng/ml) & PGE2 (1μg/ml) for 7 days. Flow sorting of MDSCs were then performed according to the expression of $CD14^+CD33^+CD11b^+$.

Cytotoxicity assays

Target cells were labelled with CellTrace FarRed dye and incubated with LILRB4 STAR-T cells or mock-T cells at the indicated effector: target (E:T) ratio in triplicates for 24h or 48h. At the end of the co-culture, cells were harvested and stained with propidium iodide (PI). PI^+CTR^+ cells were quantified by flow cytometer. Co-culture supernatants were measured for the concentration of IFN-γ, IL-2, TNF-α following the enzyme-linked immunosorbent assay kits.

To determine cytotoxicity activity of LILRB4 STAR-T cells against MM patient samples, BMMCs were first stained with antibodies against CD38, CD11b, CD14, LILRB4 to quantify the LILRB4 positive target cells in BMMCs. Then, BMMCs were co-cultured with STAR-T cells or mock-T cells for 4h at E:T ratio of 1:1 and 5:1. After incubation, the co-culture cells were stained with CD38, CD11b, CD14, LILRB4 and 7-AAD. Counting beads were added for normalization as well.

Flow cytometry analysis

Flow cytometry was performed on CantoⅡ flow cytometer (BD Biosciences) and the data were analyzed by Flowjo V10 software (Treestar). The antibodies are listed in **Table S5**.

Statistical analysis

Data analyses were performed with R language and GraphPad Prism 8.0 Software. Statistical significance was set at $P < 0.05$.

Supplemental Tables

Table. S1| The gene list of the highly expressed genes regulated by H3K27ac in cluster4

Gene	p_val	avg_logFC	avg_logExp.1	avg_logExp.2	p_val_adj	geneChr
LILRB4	0	2.17908523	2.40554514	0.22645992	0	chr19
STMN1	0	1.40553826	2.75145486	1.34591659	0	chr1
PTTG1	0	0.95213495	1.28386214	0.33172719	0	chr5
PAGE5	0	0.8527573	0.89321904	0.04046175	0	chrX
TK1	0	0.72126706	0.88658346	0.1653164	0	chr17
MCM5	0	0.65412165	0.84310093	0.18897929	0	chr22
CENPW	0	0.62891533	0.74713037	0.11821504	0	chr6
PHF19	0	0.57845067	0.69203694	0.11358627	0	chr9
PVALB	0	0.53796586	0.55888082	0.02091495	0	chr22
GINS2	0	0.53282238	0.63076266	0.09794028	0	chr16
SSX1	0	0.290379	0.30059916	0.01022016	0	chrX
MAGEB2	0	0.28337759	0.29427583	0.01089824	0	chrX
CENPH	2.74E-302	0.55582099	0.67808887	0.12226788	5.76E-298	chr5
PAFAH1B3	3.44E-301	0.80709162	0.95451379	0.14742217	7.25E-297	chr19
GAPDH	4.39E-301	2.02869199	4.72114847	2.69245649	9.25E-297	chr12
CDT1	5.20E-299	0.51638582	0.61495447	0.09856865	1.10E-294	chr16
CENPN	4.99E-296	0.56668702	0.69338616	0.12669914	1.05E-291	chr16
CRIP1	9.97E-295	2.11911896	3.14333347	1.0242145	2.10E-290	chr14
GULP1	1.84E-289	0.32850986	0.34561042	0.01710056	3.87E-285	chr2
SHCBP1	1.90E-282	0.38314151	0.43386619	0.05072469	4.00E-278	chr16
ENO1	2.74E-282	1.61850607	2.49969514	0.88118907	5.77E-278	chr1
FAM3B	2.75E-282	0.31034582	0.31738059	0.00703477	5.79E-278	chr21
ACY3	5.01E-279	0.66839987	0.76295517	0.0945553	1.05E-274	chr11
RRM2	1.29E-277	0.87093479	1.08603547	0.21510068	2.71E-273	chr2
MAD2L1	1.96E-269	0.62099465	0.82557036	0.2045757	4.13E-265	chr4
TYMS	5.49E-268	0.79456845	1.16973305	0.37516459	1.15E-263	chr18
CDC6	5.83E-265	0.39851254	0.46916167	0.07064913	1.23E-260	chr17
C19orf48	2.80E-260	0.91900105	1.2763505	0.35734945	5.89E-256	chr19
ASF1B	2.31E-259	0.41431229	0.50840515	0.09409286	4.86E-255	chr19
GMNN	6.86E-257	0.56085582	0.7075087	0.14665288	1.44E-252	chr6
CD9	1.90E-254	1.38218422	1.8881117	0.50592748	4.00E-250	chr12
TUBA1B	1.72E-253	1.72586739	3.58602697	1.86015958	3.63E-249	chr12
PCLAF	1.36E-250	1.11541067	1.72628242	0.61087175	2.85E-246	chr15
MCM7	2.34E-250	0.72937413	1.08684466	0.35747054	4.93E-246	chr7
C11orf96	7.10E-249	0.72561813	0.82765119	0.10203306	1.50E-244	chr11
ADTRP	8.92E-249	0.53174978	0.61626589	0.08451611	1.88E-244	chr6
NLRP7	3.51E-247	0.2750494	0.28101606	0.00596667	7.38E-243	chr19
POLD2	2.31E-245	0.7992543	1.0874332	0.2881789	4.87E-241	chr7
FBL	5.27E-241	1.11599251	1.62947462	0.5134821	1.11E-236	chr19

Table. S2| H3K27ac regulation in LILRB4 expression from ChIP-seq data of GSE145891

Dataset	PeakScore (MACS 2)	-log10 (Pvalue)	PeakStart	PeakEnd	annotation	distanceToTSS	GENESYMBOL
GSM4338508	42	6.23028	55171781	55178336	Promoter (<=1kb)	0	LILRB4
GSM4338510	17	4.41754	55172220	55172804	Promoter (1-2kb)	-1320	LILRB4
GSM4338514	31	5.34083	55172181	55173612	Promoter (<=1kb)	-512	LILRB4
GSM4338516	63	8.31412	55171391	55178385	Promoter (<=1kb)	0	LILRB4
GSM4338518	30	5.61436	55173013	55174228	Promoter (<=1kb)	0	LILRB4
GSM4338520	12	2.90607	55172345	55172891	Promoter (1-2kb)	-1233	LILRB4
GSM4338522	18	3.64749	55172593	55172801	Promoter (1-2kb)	-1323	LILRB4

Table. S3| The baseline clinical information of bone marrow samples used for LILRB4 STAR-T cell cytotoxicity analysis

Sample	Disease status	Treatment	Cytogenetic aberrancy
Pt1	Post-treatment	PI-based	1q21gain, del(13q)
Pt2	Post-treatment	PI-based	1q21gain, del(13q)
Pt3	ND PCL	n.a.	t(11;14)
Pt4	NDMM	n.a	del(13q)
Pt5	RRMM	PI-based	1q21gain, del(13q), t(14;unidentified)
Pt6	RRMM	PI-based	1q21gain, del(13q), t(14;unidentified)
Pt7	RRMM	PI-based, Daratumumab, BCMA-ADC	1q21gain, del(13q), t(14;unidentified)
Pt8	RRMM	PI-based, BCMA CAR-T	1q21gain, t(14;unidentified)
Pt9	RRMM	PI-based, BCMA CAR-T	1q21gain, t(4;14)

Table. S4 | The guiding RNA for LILRB4 Crispr-Cas9 knockout

Guiding RNA #	Guiding RNA sequence
sgRNA1	5′-TGTTACTATCGCAGCCCTGT-3′
sgRNA2	5′-GTAGGTCCCCCCGTGCACTG-3′
sgRNA3	5′-CCTGTGACCTCAGTGCAC GG-3‘

Table. S5 | Antibodies for flowcytometry analysis

Antibody	Clone	Company	Order number
anti-hCD19-BV421	UCHT1	BioLegend	300452
anti-hCD56-FITC	TULY56	eBioscience	4299203
anti-hCD38-PE-Cy7	HIT2	BioLegend	303516
anti-hCD138-PE	MI15	BD Biosciences	552026
anti-hCD45-Percp	2D1	BD Biosciences	347464
anti-hLILRB4-APC	ZM4.1	BioLegend	333016
anti-hCD11b-PE-Cy7	M1/70	BioLegend	101216
anti-hCD14-APC-Cy7	HCD14	BioLegend	325619
anti-hCD15-FITC	MMA	BioLegend	394706
anti-hCD33-PE	WM53	BD Biosciences	555450
anti-HLA-DR-Pacific-blue	LN3	BioLegend	327016
anti-mCD45-PE-Cy7	30-F11	BioLegend	103114
anti-mCD11b-APC	M1/70	eBioscience	17-0112-82
anti-mGr1-PE	RB6-8C5	BioLegend	108407
Live/Dead Cell Stain Kit		ThermoFisher Scientific	L34965

References

1. Dobin A, Davis CA, Schlesinger F et al. STAR: ultrafast universal RNA-seq aligner. Bioinformatics (Oxford, England). 2013 Jan 1;29(1):15-21.

2. Guo W, Wang D, Wang S et al. scCancer: a package for automated processing of single-cell RNA-seq data in cancer. Brief Bioinform. 2021 May 20;22(3).

3. Korsunsky I, Millard N, Fan J et al. Fast, sensitive and accurate integration of single-cell data with Harmony. Nat Methods. 2019 Dec;16(12):1289-1296.

4. Butler A, Hoffman P, Smibert P et al. Integrating single-cell transcriptomic data across different conditions, technologies, and species. Nat Biotechnol. 2018 Jun;36(5):411-420.

5. Stuart T, Butler A, Hoffman P et al. Comprehensive Integration of Single-Cell Data. Cell. 2019 Jun 13;177(7):1888-1902.e21.

6. Dominguez Conde C, Xu C, Jarvis LB et al. Cross-tissue immune cell analysis reveals tissue-specific features in humans. Science. 2022 May 13;376(6594):eabl5197.

7. Zheng L, Qin S, Si W et al. Pan-cancer single-cell landscape of tumor-infiltrating T cells. Science. 2021 Dec 17;374(6574):abe6474.

8. Zhang Y, Wang S, Zhang J et al. Elucidating minimal residual disease of paediatric B-cell acute lymphoblastic leukaemia by single-cell analysis. Nat Cell Biol. 2022 Feb;24(2):242-252.

9. Alameda D, Goicoechea I, Vicari M et al. Tumor cells in light-chain amyloidosis and myeloma show distinct transcriptional rewiring of normal plasma cell development. Blood. 2021 Oct 28;138(17):1583-1589.

10. Qiu X, Mao Q, Tang Y et al. Reversed graph embedding resolves complex single-cell trajectories. Nature methods. 2017 Oct;14(10):979-982.
11. Rai A, Greening DW, Chen M et al. Exosomes Derived from Human Primary and Metastatic Colorectal Cancer Cells Contribute to Functional Heterogeneity of Activated Fibroblasts by Reprogramming Their Proteome. Proteomics. 2019 Apr;19(8):e1800148.
12. Han H, Cho JW, Lee S et al. TRRUST v2: an expanded reference database of human and mouse transcriptional regulatory interactions. Nucleic Acids Res. 2018 Jan 4;46(D1):D380-d386.
13. Walker BA, Mavrommatis K, Wardell CP et al. Identification of novel mutational drivers reveals oncogene dependencies in multiple myeloma. Blood. 2018 Aug 9;132(6):587-597.
14. Newman AM, Steen CB, Liu CL et al. Determining cell type abundance and expression from bulk tissues with digital cytometry. Nat Biotechnol. 2019 Jul;37(7):773-782.
15. Patel AP, Tirosh I, Trombetta JJ et al. Single-cell RNA-seq highlights intratumoral heterogeneity in primary glioblastoma. Science. 2014 Jun 20;344(6190):1396-401.
16. Zhang H, Meltzer P, Davis S. RCircos: an R package for Circos 2D track plots. BMC Bioinformatics. 2013 Aug 10;14:244.
17. Andreatta M, Carmona SJ. STACAS: Sub-Type Anchor Correction for Alignment in Seurat to integrate single-cell RNA-seq data. Bioinformatics. 2021 May 5;37(6):882-884.
18. Alshetaiwi H, Pervolarakis N, McIntyre LL et al. Defining the emergence of myeloid-derived suppressor cells in breast cancer using single-cell transcriptomics. Sci Immunol. 2020 Feb 21;5(44).
19. Cheng S, Li Z, Gao R et al. A pan-cancer single-cell transcriptional atlas of tumor infiltrating myeloid cells. Cell. 2021 Feb 4;184(3):792-809.e23.
20. Andreatta M, Corria-Osorio J, Müller S et al. Interpretation of T cell states from single-cell transcriptomics data using reference atlases. Nature communications. 2021 May 20;12(1):2965.
21. Sun Y, Wu L, Zhong Y et al. Single-cell landscape of the ecosystem in early-relapse hepatocellular carcinoma. Cell. 2021 Jan 21;184(2):404-421.e16.
22. Robinson MD, McCarthy DJ, Smyth GK. edgeR: a Bioconductor package for differential expression analysis of digital gene expression data. Bioinformatics (Oxford, England). 2010 Jan 1;26(1):139-40.
23. Yu T, Du C, Ma X et al. Polycomb-like Protein 3 Induces Proliferation and Drug Resistance in Multiple Myeloma and Is Regulated by miRNA-15a. Mol Cancer Res. 2020 Jul;18(7):1063-1073.
24. Yu Z, Wei X, Liu L et al. Indirubin-3'-monoxime acts as proteasome inhibitor: Therapeutic application in multiple myeloma. EBioMedicine. 2022 Apr;78:103950.

Suppl. Fig. 1

A

MM sample No.	S8	S12	S15	S24	S1	S2	S3	S4	S5	S16	S25	S27
Myeloma type												
Ig type	IgG	IgA	light chain	IgG	light chain	IgG	IgA	IgA	IgG	IgG	IgA	IgG
light chain type	κ	λ	κ	κ	λ	κ	κ	κ	κ	κ	λ	κ
Internetional Staging System												
ISS III	III	III	III	III	III	I	III	I	II	III	III	III
R-ISS	II	II	III	III	III	I	II	II	II	II	III	III
LDH (High)			■	■								
Cytogenetic aberrancy												
1q+	■	■	■	■	■			■	■		■	
del(17p)			■									
t(4;14)					■			■	■		■	
Treatment class												
VRD regimen	■	■	■	■	■	■	■	■	■	■	■	■
Best response	MR	PR	NR	VGPR	sCR	VGPR	CR	VGPR	PR	PR	CR	CR
Early mortality in 24 months	■	■	■	■								

Red: positive, Blank: negative

B

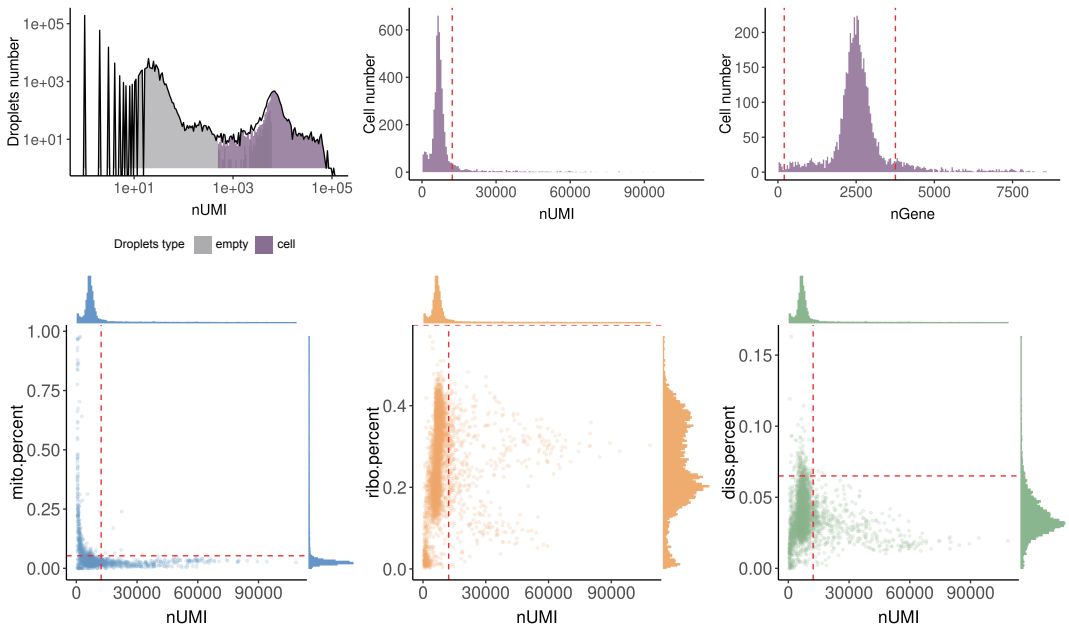

C

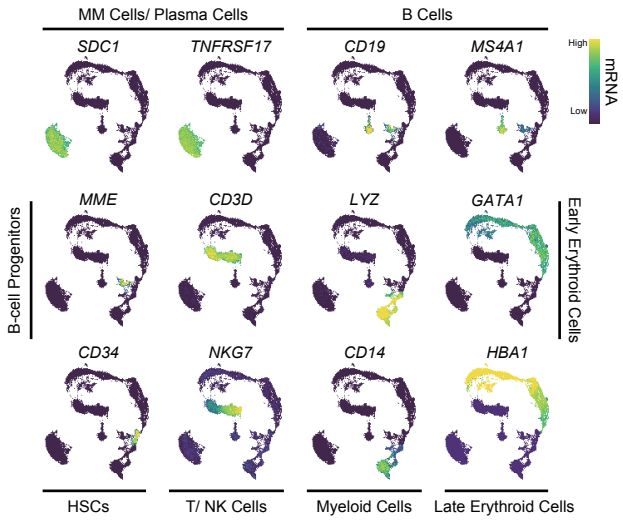

D

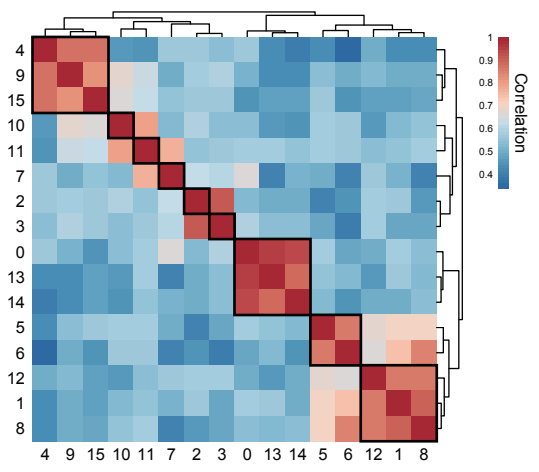

Fig. S1 | The baseline characteristics of MM patients and quality control of scRNA-seq data

(A) Diagram showing the baseline characteristics of multiple myeloma (MM) patients. Red indicates positive and blank indicates negative.

(B) Bar plots showing filtering criteria for sequenced cells, including unique molecular identifier (UMI) count, gene count, mitochondrial gene proportion, ribosomal gene proportion, and percent of dissociation-related genes.

(C) Uniform manifold approximation and projection (UMAP) plots showing the expression of marker genes in the indicated cell types. The labeled bars represent the specific cell types.

(D) Heatmap illustrating the correlation between each cell cluster. The black frame indicates cell clusters of the same cell annotation.

Suppl. Fig. 2

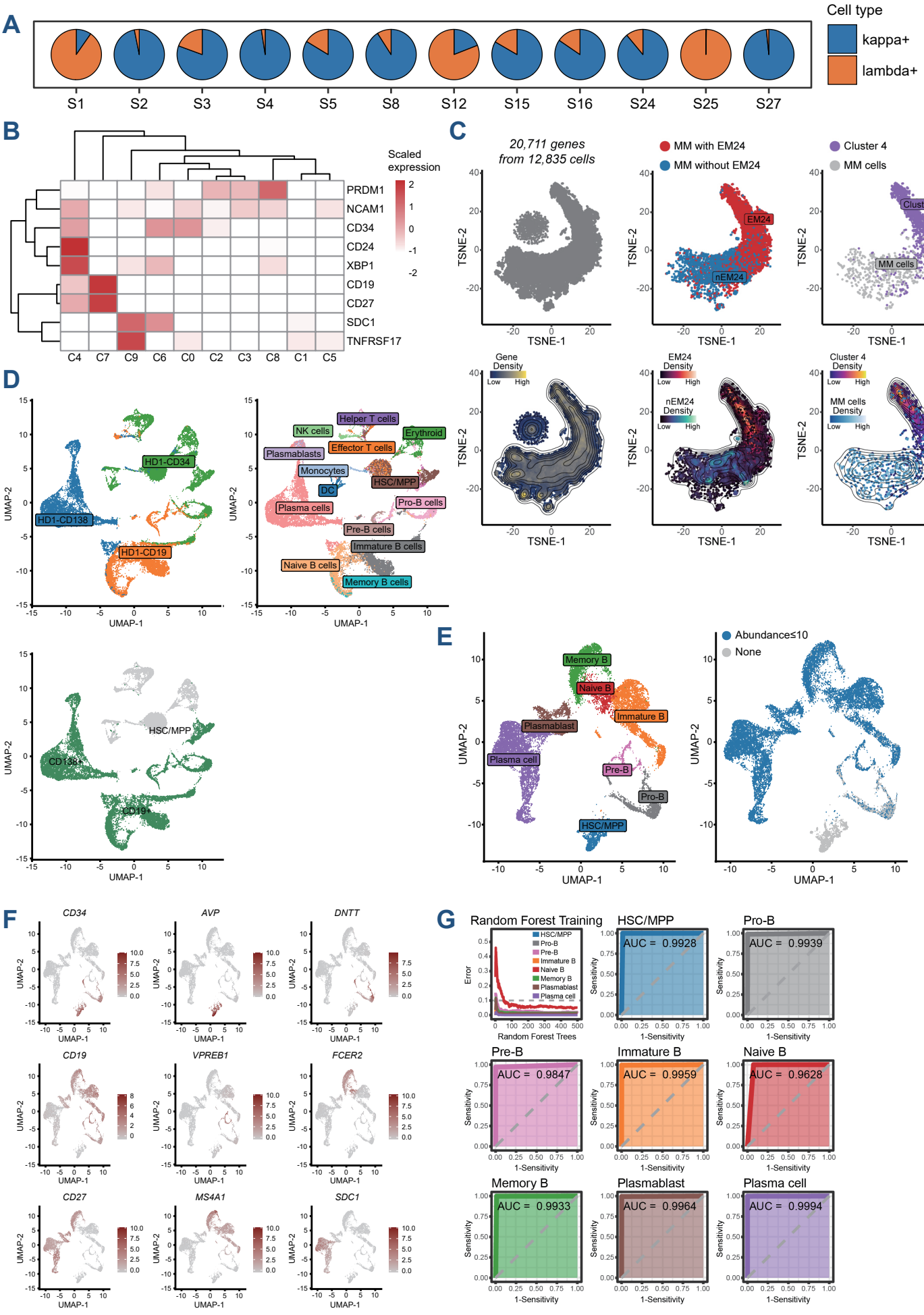
A
Cell type
kappa+
lambda+
S1
S2
S3
S4
S5
S8
S12
S15
S16
S24
S25
S27
B
Scaled expression
PRDM1
NCAM1
CD34
CD24
XBP1
CD19
CD27
SDC1
TNFRSF17
C4
C7
C9
C6
C0
C2
C3
C8
C1
C5
C
20,711 genes from 12,835 cells
MM with EM24
MM without EM24
Cluster 4
MM cells
EM24
nEM24
Gene Density
EM24 Density
nEM24 Density
Cluster 4 Density
MM cells Density
TSNE-1
TSNE-2
D
HD1-CD34
HD1-CD138
HD1-CD19
Helper T cells
NK cells
Erythroid
Effector T cells
Plasmablasts
Monocytes
HSC/MPP
DC
Pro-B cells
Plasma cells
Pre-B cells
Immature B cells
Naive B cells
Memory B cells
CD138+
CD19+
UMAP-1
UMAP-2
E
Memory B
Naive B
Immature B
Plasmablast
Plasma cell
Pre-B
Pro-B
HSC/MPP
Abundance≤10
None
F
CD34
AVP
DNTT
CD19
VPREB1
FCER2
CD27
MS4A1
SDC1
G
Random Forest Training
Error
Random Forest Trees
HSC/MPP
Pro-B
Pre-B
Immature B
Naive B
Memory B
Plasmablast
Plasma cell
AUC = 0.9928
AUC = 0.9939
AUC = 0.9847
AUC = 0.9959
AUC = 0.9628
AUC = 0.9933
AUC = 0.9964
AUC = 0.9994
Sensitivity
1-Sensitivity

Fig. S2 | Plasma-cell analysis of scRNA-seq data

(A) Pie charts showing the proportion of kappa$^+$ and lambda$^+$ plasma cells in each patient.

(B) Heatmap showing the expression of plasma-cell marker gene in each plasma-cell cluster.

(C) T-distributed stochastic neighbor embedding (tSNE) plots (top panel) and density (bottom panel) plots illustrating the topology of sequenced genes from plasma cells. Each point indicates one gene. All genes are shown on the left. The up-regulated genes in patients with early death (EM24) (red) and patients without early death (nEM24) (blue) are shown in the middle. The up-regulated genes in cluster 4 (purple) and other multiple myeloma (MM) cells (gray) are shown on the right.

Uniform manifold approximation and projection (UMAP) plots illustrating cell origin (left), cell annotation (middle), and selected cells for downstream analysis (right) of integrated CD34$^+$, CD19$^+$, and CD138$^+$ cells from integrated outsourced data. HD: healthy individual, HSC: hematopoietic stem cells, MPP: multipotent blood progenitors.

(D) UMAP plots showing the cell annotation (left) and BCR expression pattern (right) of CD34$^+$, CD19$^+$, and CD138$^+$ cells from integrated outsourced data.

(E) UMAP plots showing the expression of marker genes of plasma-cell lineage in integrated CD34$^+$, CD19$^+$, and CD138$^+$ cells.

(F) Line plot and receiver operating characteristic plots showing the performance of plasma-cell lineage classifier by random forest model. AUC: area under the curve.

Suppl. Fig. 3

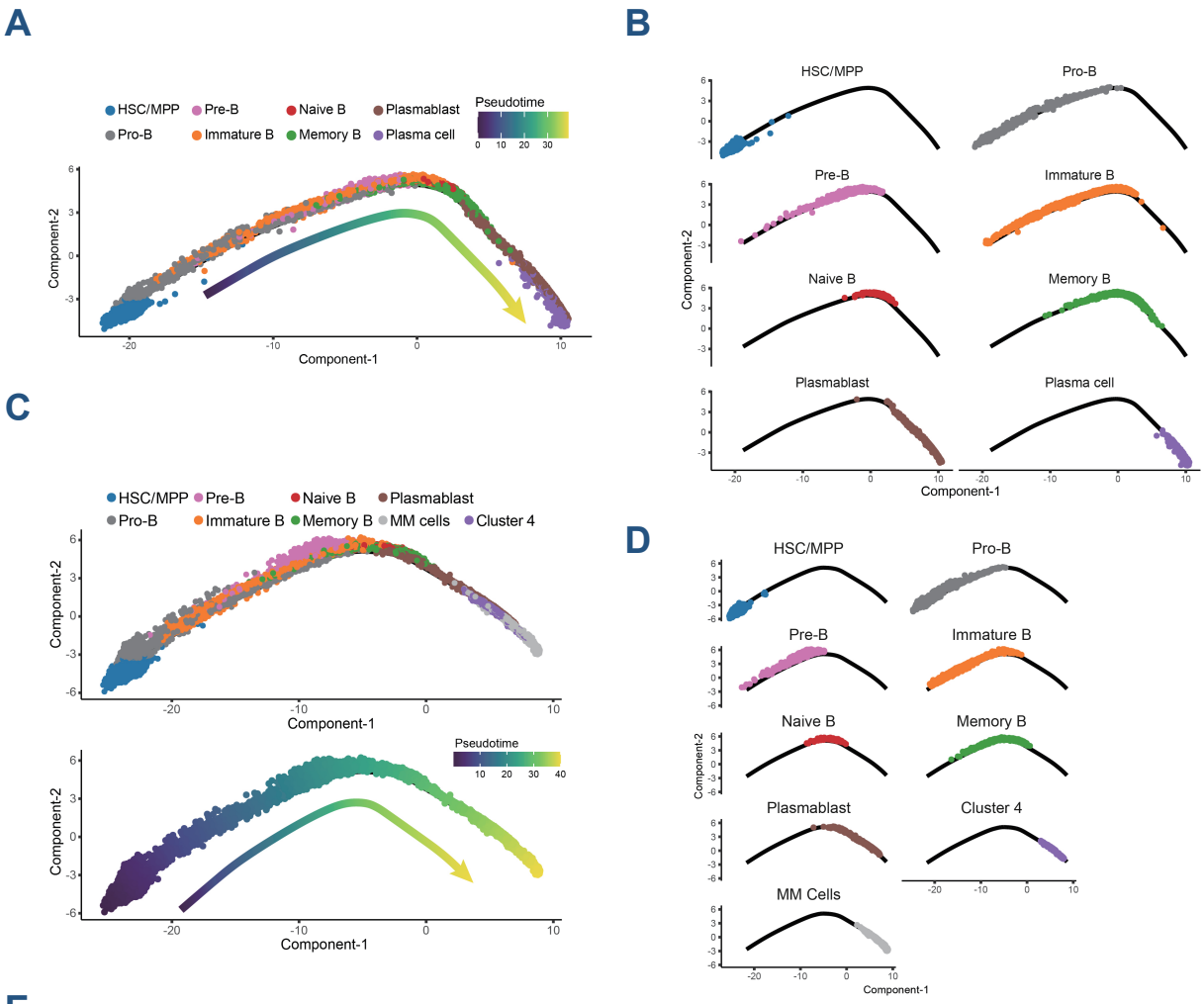
A
HSC/MPP
Pre-B
Naive B
Plasmablast
Pro-B
Immature B
Memory B
Plasma cell
Pseudotime
Component-1
Component-2
B
HSC/MPP
Pro-B
Pre-B
Immature B
Naive B
Memory B
Plasmablast
Plasma cell
C
MM cells
Cluster 4
D
Cluster 4
MM Cells
E
REACTOME_SIGNALING_BY_NOTCH
NES: 1.14
FDR: 0.036
REACTOME_SIGNALING_BY_HEDGEHOG
NES: 1.27
FDR: 0.000
GOBP_WNT_SIGNALING_PATHWAY
NES: 1.21
FDR: 0.012
GOBP_STEM_CELL_DIFFERENTIATION
NES: 1.18
FDR: 0.018
Enrichment score (ES)
sC4
others

Fig. S3 | Plasma-cell differentiation trajectory analysis

(A) Pseudotime-ordered trajectory of plasma-cell lineage using integrated $CD34^+$, $CD19^+$, and $CD138^+$ cells. HSC: hematopoietic stem cells, MPP: multipotent blood progenitors.

(B) The distribution of plasma-cell lineage during the trajectory using integrated $CD34^+$, $CD19^+$, and $CD138^+$ cells. Cells are labeled by colors.

(C) Pseudotime-ordered trajectory of plasma-cell lineage involved cluster 4 and other multiple myeloma (MM) cells. Plasma-cell lineage (top) and pseudotime order (bottom) are labeled by colors.

(D) The distribution of MM-cell clusters during the plasma-cell lineage differentiation trajectory. Cells are labeled by colors.

(E) Enrichment plots showing the enriched stemness-related signaling pathways in sub-C4.

Suppl. Fig. 4

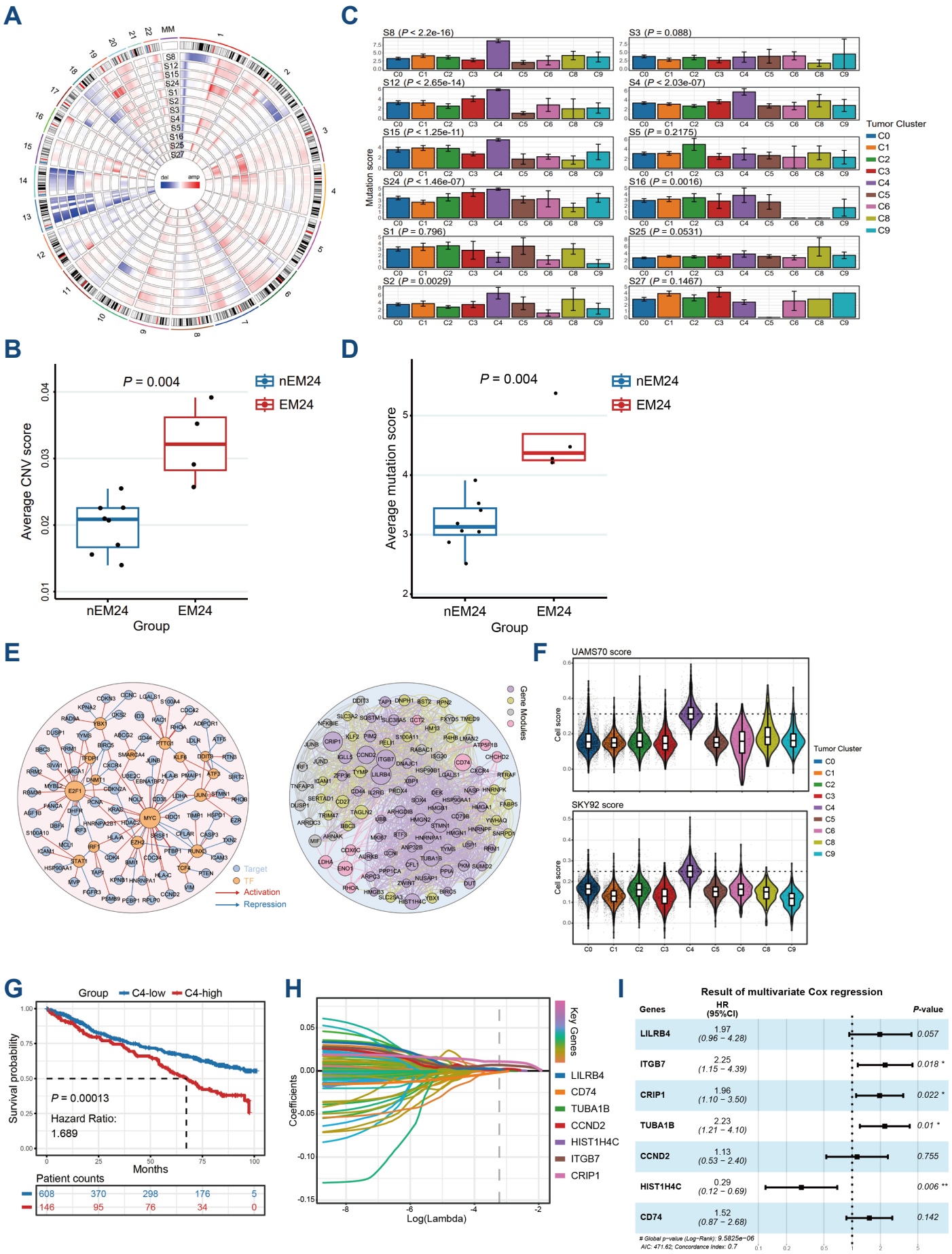
A
B
C
D
E
F
G
H
I
P = 0.004
nEM24
EM24
Group
Average CNV score
Average mutation score
Mutation score
Tumor Cluster
C0
C1
C2
C3
C4
C5
C6
C8
C9
UAMS70 score
SKY92 score
Cell score
Target
TF
Activation
Repression
Gene Modules
Group C4-low C4-high
Survival probability
P = 0.00013
Hazard Ratio:
1.689
Months
Patient counts
608 370 298 176 5
146 95 76 34 0
Coefficients
Log(Lambda)
Key Genes
LILRB4
CD74
TUBA1B
CCND2
HIST1H4C
ITGB7
CRIP1
Result of multivariate Cox regression
Genes
HR (95%CI)
P-value
LILRB4 1.97 (0.96 – 4.28) 0.057
ITGB7 2.25 (1.15 – 4.39) 0.018 *
CRIP1 1.96 (1.10 – 3.50) 0.022 *
TUBA1B 2.23 (1.21 – 4.10) 0.01 *
CCND2 1.13 (0.53 – 2.40) 0.755
HIST1H4C 0.29 (0.12 – 0.69) 0.006 **
CD74 1.52 (0.87 – 2.68) 0.142
Global p-value (Log-Rank): 9.5825e-06
AIC: 471.62; Concordance Index: 0.7

Fig. S4 | Genomic features of sub-cluster 4

(A) Circular genomic map illustrating the copy number variations (CNV) in each multiple myeloma (MM) patient. Each lane indicates one patient and the outmost lane indicates chromosome structure. Red represents amplification and blue represents deletion.

(B) Box plot showing the average CNV score between patients with early death (EM24) and patients without early death (nEM24).

(C) Bar plots showing the mutation score of each tumor cluster in each patient.

(D) Box plot showing the mutation score between EM24 patients and nEM24 patients.

(E) (Left) Regulatory network of major transcription factors (TF) and target genes up-regulated in cluster 4 compared with other MM cells. The point size indicates the edge numbers of TF. (Right) Gene co-expression network displaying the top gene modules specific to cluster 4. The point size indicates the gene fold change in cluster 4 versus other MM cells. The lines connect significantly correlated genes.

(F) Violin plots showing the cell score of UAMS70 and SKY92 in MM cell clusters.

(G) Kaplan-Meier curve showing the overall survival of 754 MM patients with a high or low proportion of sub-C4 in the MMRF-CoMMpass dataset. Log-rank test was applied in the comparison between groups.

(H) Line chart showing the least absolute shrinkage and selection operator (lasso) coefficient profiles of the 170 risk factors against log(Lambda).

(I) Forest plot showing the hazard ratio of 7 genes by multivariate cox regression in MMRF-CoMMpass cohort.

Suppl. Fig. 5

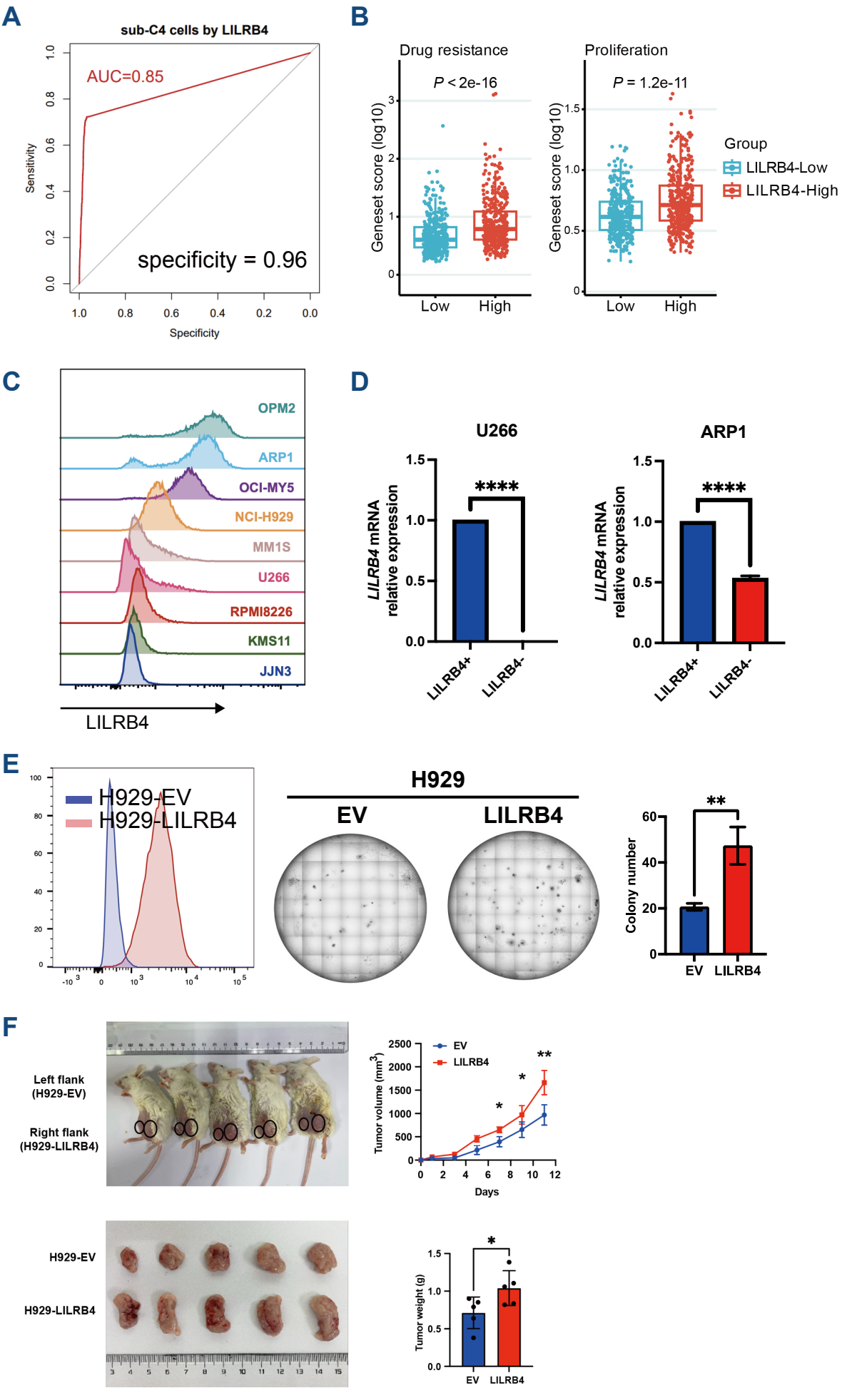
A
sub-C4 cells by LILRB4
AUC=0.85
specificity = 0.96
Sensitivity
Specificity
B
Drug resistance
P < 2e-16
Proliferation
P = 1.2e-11
Geneset score (log10)
Low
High
Group
LILRB4-Low
LILRB4-High
C
OPM2
ARP1
OCI-MY5
NCI-H929
MM1S
U266
RPMI8226
KMS11
JJN3
LILRB4
D
U266
ARP1
LILRB4 mRNA relative expression
****
LILRB4+
LILRB4-
E
H929-EV
H929-LILRB4
H929
EV
LILRB4
Colony number
**
F
Left flank (H929-EV)
Right flank (H929-LILRB4)
Tumor volume (mm3)
Days
H929-EV
H929-LILRB4
Tumor weight (g)

Fig. S5 | LILRB4 is a biomarker of aggressive MM

(A) Receiver operating characteristic (ROC) curve showing the specificity of LILRB4 expression in sub-C4. AUC: area under the curve.

(B) The score of drug-resistance and proliferation geneset between LILRB4-low and LILRB4-high patients in MMRF-CoMMpass cohort.

(C) Flow cytometry detection of LILRB4 in multiple multiple myeloma (MM) cell lines.

(D) LILRB4 mRNA expression of $LILRB4^{+}$ and $LILRB4^{-}$ cells. Unpaired *t* test, two-tailed, ****P<0.0001

(E) (Left) Flow cytometry detection of LILRB4 in H929-EV and H929-LILRB4 cells. (Right) Colony formation assay of H929-LILRB4 cells relative to H929-EV cells. Unpaired *t* test, two-tailed, **P<0.01.

(F) The H929-EV and H929-LILRB4 cells were injected subcutaneously into the left and right flank of the same mouse. Bar plots showing the statistical result of tumor weight between H929-EV and H929-LILRB4 group with unpaired *t* test, two-tailed, *P < 0.05, **P<0.01.

Suppl. Fig. 6

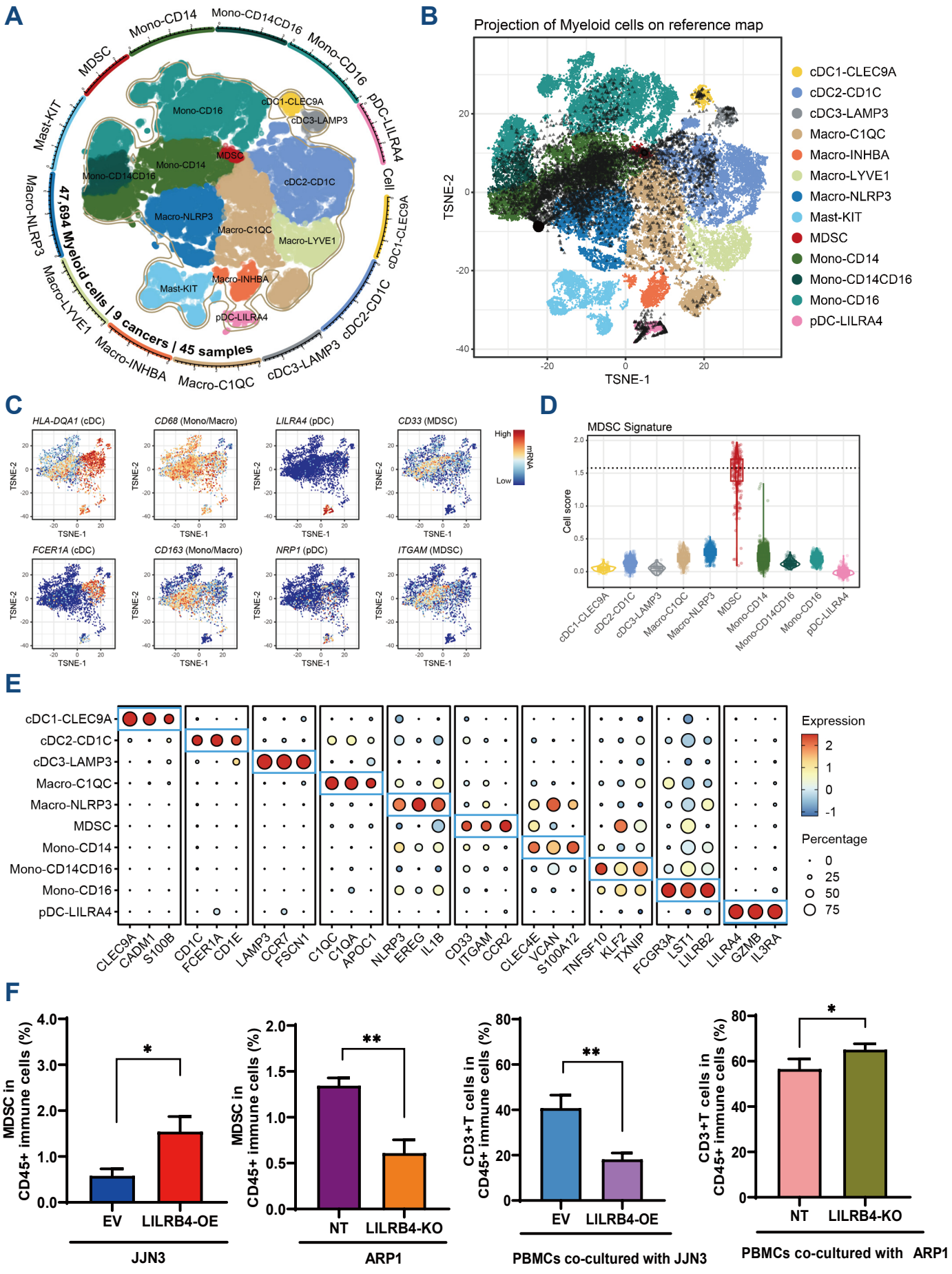
A
Mono-CD14
Mono-CD14CD16
Mono-CD16
pDC-LILRA4
cDC1-CLEC9A
cDC2-CD1C
cDC3-LAMP3
Macro-C1QC
Macro-INHBA
Macro-LYVE1
Macro-NLRP3
Mast-KIT
MDSC
47,694 Myeloid cells | 9 cancers | 45 samples
B
Projection of Myeloid cells on reference map
TSNE-1
TSNE-2
C
HLA-DQA1 (cDC)
CD68 (Mono/Macro)
LILRA4 (pDC)
CD33 (MDSC)
FCER1A (cDC)
CD163 (Mono/Macro)
NRP1 (pDC)
ITGAM (MDSC)
High
Low
mRNA
D
MDSC Signature
Cell score
E
Expression
Percentage
CLEC9A
CADM1
S100B
CD1C
FCER1A
CD1E
LAMP3
CCR7
FSCN1
C1QC
C1QA
APOC1
NLRP3
EREG
IL1B
CD33
ITGAM
CCR2
CLEC4E
VCAN
S100A12
TNFSF10
KLF2
TXNIP
FCGR3A
LST1
LILRB2
LILRA4
GZMB
IL3RA
F
MDSC in CD45+ immune cells (%)
EV
LILRB4-OE
JJN3
NT
LILRB4-KO
ARP1
CD3+T cells in CD45+ immune cells (%)
PBMCs co-cultured with JJN3
PBMCs co-cultured with ARP1

Fig. S6 | Myeloid cell annotation and signature gene expression

(A) Points plot showing integrated myeloid cell map for reference, including 47,694 cells from 45 samples of 9 cancers.

(B) T-distributed stochastic neighbor embedding (tSNE) plot showing the distribution of annotated myeloid cells. Cell annotations are labeled by colors.

(C) TSNE plots showing the marker gene expression for the major lineages of myeloid cells.

(D) Violin plot showing the myeloid-derived suppressive cell (MDSC) signature scores in myeloid cell types.

(E) Bubble heatmap showing expression levels of selected signature genes in myeloid cells. Dot size indicates fraction of expressing cells, colored based on normalized expression levels.

(F) Bar plots showing the proportion of MDSCs or $CD3^+$ T cells in peripheral blood mononuclear cells (PBMCs) after co-culturing with multiple myeloma (MM) cells with different LILRB4 level respectively. The statistical results were tested with unpaired *t* test, two-tailed, $*P < 0.05$, $**P<0.01$.

Suppl. Fig. 7

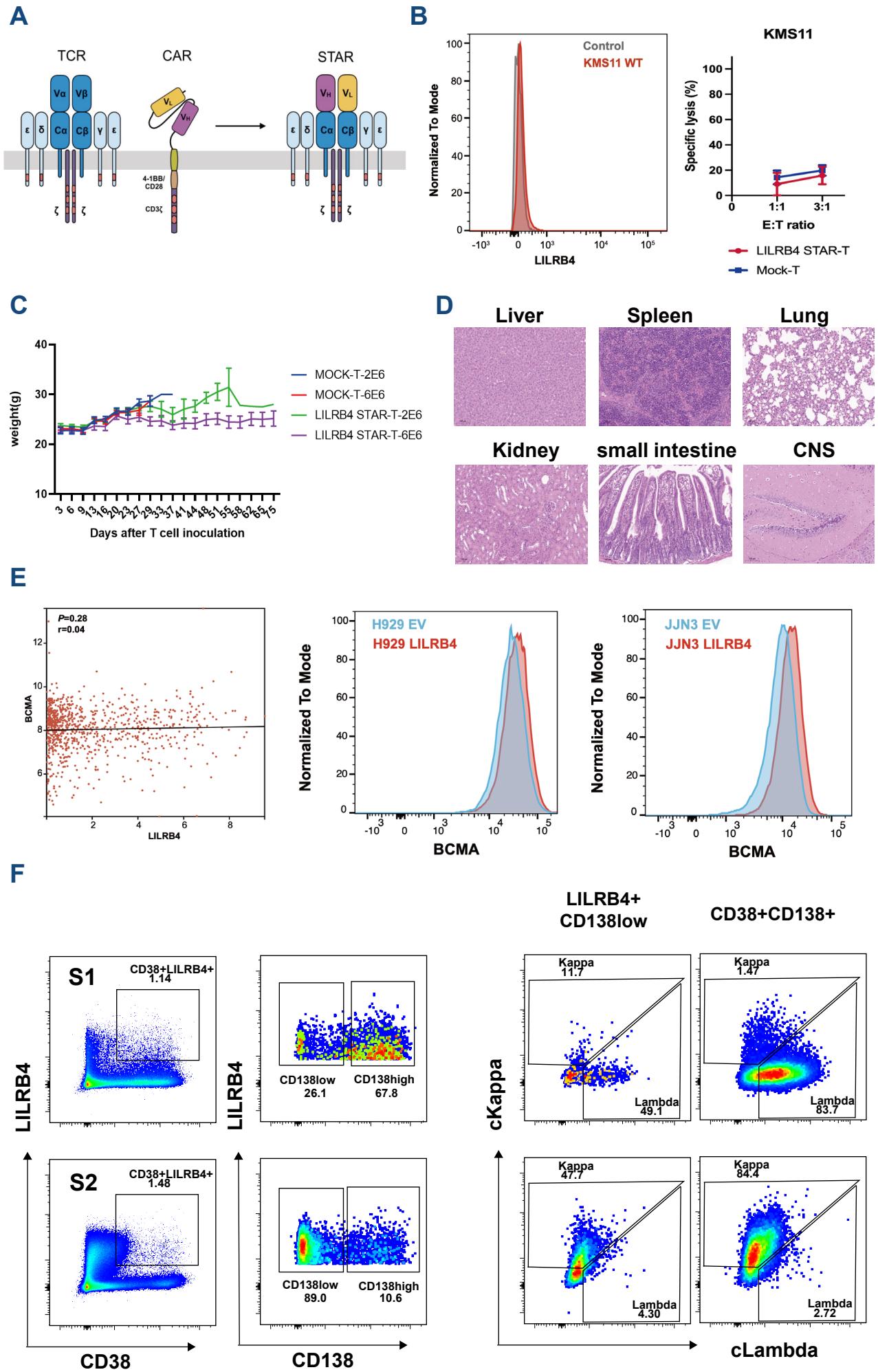
A
TCR
CAR
STAR
Vα
Vβ
Cα
Cβ
ε
δ
γ
ζ
VL
VH
4-1BB/
CD28
CD3ζ
B
Control
KMS11 WT
Normalized To Mode
LILRB4
KMS11
Specific lysis (%)
E:T ratio
1:1
3:1
LILRB4 STAR-T
Mock-T
C
weight(g)
Days after T cell inoculation
MOCK-T-2E6
MOCK-T-6E6
LILRB4 STAR-T-2E6
LILRB4 STAR-T-6E6
D
Liver
Spleen
Lung
Kidney
small intestine
CNS
E
P=0.28
r=0.04
BCMA
LILRB4
H929 EV
H929 LILRB4
JJN3 EV
JJN3 LILRB4
F
LILRB4+
CD138low
CD38+CD138+
S1
CD38+LILRB4+
1.14
CD138low
26.1
CD138high
67.8
Kappa
11.7
Lambda
49.1
Kappa
1.47
Lambda
83.7
S2
CD38+LILRB4+
1.48
CD138low
89.0
CD138high
10.6
Kappa
47.7
Lambda
4.30
Kappa
84.4
Lambda
2.72
CD38
CD138
cKappa
cLambda

Fig. S7 | LILRB4 STAR-T cell pre-clinical study in MM

(A) Schematic construct of LILRB4 synthetic T cell receptor and antigen receptor (STAR)-T cells.

(B) LILRB4 STAR-T cell cytotoxicity assay towards LILRB4$^-$ KMS11 multiple myeloma (MM) cells.

(C) Line chart illustrating the subcutaneous tumor weight in MM xenograft mice after treating with mock-T cells or LILRB4 STAR-T cells.

(D) Hematoxylin-eosin staining of multiple organs from MM xenograft mice after treating with LILRB4 STAR-T cells.

(E) (Left) Correlation analysis of *BCMA* and *LILRB4* mRNA expression in GSE2658 dataset. (Right) Flow cytometry detection of BCMA in LILRB4-overexpressed MM cells.

(F) Exemplary plot for light chain restriction analysis of CD38$^+$LILRB4$^+$CD138^{low} cell cluster and CD38$^+$CD138$^+$ cell cluster from the same patient by flow cytometry detection.